A high–order algorithm for obstacle scattering in three dimensions

M. Ganesh* I.G. Graham†

Dedicated to Professor Ian H. Sloan on the occasion of his 65th birthday.

Abstract

In this work we describe, implement and analyse in detail a high–order fully discrete spectral algorithm for solving the Helmholtz equation exterior to a bounded (sound–soft, sound–hard or absorbing) obstacle in three space dimensions, with Dirichlet, Neumann or Robin (impedance) boundary conditions. Our algorithm may be thought of as a discrete Galerkin method, but it is also equivalent to a Nyström method after a simple transformation. We test our algorithm with extensive computational experiments on a variety of three dimensional smooth and non–smooth obstacles with conical singularities. Our tests include the computation of scattered and far fields induced by incident plane waves. Our method is shown to be very accurate for scattering from surfaces which are globally parameterised by spherical coordinates, and tests show that it performs very much better than several of the well-established fast algorithms for obstacle scattering on a range of such surfaces, even some which are non-smooth. Further, we prove superalgebraic convergence of the scattered and far fields obtained using our algorithm in the case of smooth scatterers.

Keywords: Acoustic scattering; sound–soft, sound–hard, absorbing obstacles; exterior Helmholtz problems; boundary integral equations; spherical harmonics; quadrature.

Mathematical Subject Classifications: 45B05, 65R20

*Department of Mathematical and Computer Sciences, Colorado School of Mines, Golden, CO 80401. mganesh@mines.edu

†Department of Mathematical Sciences, University of Bath, Bath, BA2 7AY, UK. I.G.Graham@bath.ac.uk

1 Introduction

In this paper, we present a high–order algorithm for solving the Helmholtz equation defined in an unbounded region, composed of the exterior of a bounded connected obstacle in $\mathbb{R}^3$, with Dirichlet, Neumann or Robin (impedance) boundary conditions. It is well known that efficient computational schemes for such problems play a significant rôle in scattering theory [7, 8, 9, 18]. Our algorithm is based on the boundary integral method and has the usual advantage over domain discretisation schemes that only the finite boundary has to be discretised and the radiation condition is satisfied automatically. Domain truncation or infinite elements (e.g. [12]) can thus be avoided.

The spectral algorithm discussed in the present paper is restricted to the class of obstacles with surfaces that can be described globally in spherical coordinates. When the surface is smooth, our algorithm attains exponential convergence by exploiting the smoothness and the spherical coordinate system in a special way. As we shall see, relatively few degrees of freedom are required to obtain good accuracy on the boundary or in the exterior domain, or to compute the practically important far field pattern. In particular, our numerical experiments on spherical scatterers (see §4) show that, for frequencies in the resonance region (i.e. for obstacles with size close to one wavelength) very accurate far field approximate solutions (for a fixed incident and observed direction) can be computed in less than one minute of CPU time (on a moderate computing platform) and for high frequency scattering (with wavelengths down to 0.04 times the size of obstacles), accurate solutions (i.e. RMS error about 0.001 %) can be computed in about ten hours of CPU time. Resonance region calculations are of particular use for inverse scattering ([8, p. 105]).

We compare our algorithm with some of the most powerful recent algorithms for scattering [3, 4, 6, 20]. In [3, 4] the Bruno–Kunyansky sound–soft acoustic scattering algorithm has been computationally demonstrated to be very competitive with the fast multipole algorithm FISC [20] and the high–order Nyström algorithm FastScat [6], used in electromagnetic scattering. We compare our algorithm with that of Bruno–Kunyansky (for all the smooth and non-smooth obstacles considered in [3, 4, 5]) and demonstrate very competitive accuracy and efficiency of our algorithm in §4. A common feature of our method and that of Bruno–Kunyansky is the use of spherical coordinates; globally in our case and locally in [3, 4]. Due to our assumption that the surface is globally parametrisable, we are able to treat the singularities in the weakly singular integrals analytically using a singularity division technique.

In the appendix to this paper we prove the superalgebraic convergence of our algorithm in the case of smooth surfaces. In §4 we demonstrate also that our algorithm can also be used effectively for non–smooth obstacles (provided they have an appropriate global parametrisation). The non-smooth objects used in our experiments feature conical singularities and can be found in the list of benchmark radar targets suggested in [23]. The theoretical restriction to smooth objects may not be so much of a disadvantage in the context of inverse scattering [8], where general qualitative information about obstacles is of greater importance than finer details of obstacles such as corners and edges. Moreover, when the boundary–integral and finite–element methods are coupled across an artificial surface, this surface can be chosen to be smooth, and then the discretisation proposed here would be very appropriate. (See [14] for such an approach in two dimensions.)

We would like to remark that the restriction to surfaces which can be globally parametrised by spherical coordinates is here rather essential. The extension of our method to more general geometries would require covering the surface with several coordinate charts. The extension of our method to this setting raises a number of technical problems, both in the formulation of an extended algorithm and in its error analysis.

A basic theory for the discretisation proposed here was given in [13], which in turn built on the results in [11, 22]. However, most practical details required for obstacle scattering, such as an algorithm for computing the far field and the exterior scattered field were omitted in [13]. These details are part of the present paper. In addition, an important component of our algorithm is the efficient computation of rotated spherical harmonics. In [22] (see also [8, p. 84]), such computations were based on the idea of computing Fourier coefficients of rotated harmonics using a high–order quadrature rule. In [13] a simple explicit formula which avoided such quadratures was presented. However the formula in [13] turns out not to be useful in practice for high degree spherical harmonics (e.g. degree 25 or above), since it contains many terms of almost equal size but with differing sign and thus suffers from cancellation error. We overcome this difficulty by deriving (in §3.3) an alternative formula which avoids this cancellation problem. This formula is crucial for the success of our method in the high-frequency examples.

In the present paper we provide a full specification of our obstacle scattering algorithm, extensive numerical experiments and additional theoretical results which are needed to describe the computation of approximate solutions exterior to the scatterer and the far field. We also discuss the implementation of general boundary conditions: the boundary integral method in [13] is restricted to the Dirichlet case.

For part of the long history of spectral boundary integral methods using spherical functions, we refer to [1, 8, 10, 11, 13, 15, 16, 22] and for background on integral equations in scattering theory we refer to [7, 8, 18]. For a three dimensional exterior Helmholtz problem, a fully discrete spectral method using a singularity division technique was introduced (but not analysed) in [22]. In [22], computational results mainly for frequencies in the resonance region are given but without CPU time details. Our algorithm leads to only half the size of the linear system in [22]. A three dimensional spectral method with a singularity subtraction technique was investigated in [15] and recently, the algorithm of [15] was used in [16] for a different boundary integral formulation of the exterior problem. In [15, 16] only a semi–discrete version of the actually implemented method was analysed. Further, only low frequency computational results are given in [15, 16]. Since our algorithm requires only about a minute of a CPU time to reach high accuracy for low frequencies, much faster than the CPU times reported in [15, 16], we avoid detailed comparison with methods in [15, 16, 22] and instead focus mainly on a comparison with [3, 4].

In this work we are interested in computing an approximation to the *radiating solution* u of the exterior Helmholtz equation

$$\triangle u(\mathbf{x}) + k^2 u(\mathbf{x}) = 0, \qquad \mathbf{x} \in \mathbb{R}^3 \setminus \bar{D}, \tag{1.1}$$

where $D \subset \mathbb{R}^3$ is assumed to be a bounded connected domain with boundary ∂D and a connected complement $\mathbb{R}^3 \setminus \bar{D}$. (We will give precise requirements on the surface ∂D in

the next section.) Here, $k > 0$ is called the wavenumber and we use the standard notion of *radiating solution* [7, 8, 18], i.e. u satisfies the Sommerfeld radiation condition

$$\lim_{r\to\infty} r\left(\partial u/\partial r - iku\right) = 0, \tag{1.2}$$

where $r = |\mathbf{x}|$ and the limit is assumed to hold uniformly in all directions $\mathbf{x}/|\mathbf{x}|$. Assuming that (1.1) has a unique radiating solution, under appropriate regularity assumptions, by Green's theorem, u can be represented as [8, Theorem 2.4]:

$$u(\mathbf{x}) = \int_{\partial D} \frac{\partial \Phi(\mathbf{x},\mathbf{y})}{\partial n(\mathbf{y})} u(\mathbf{y}) ds(\mathbf{y}) - \int_{\partial D} \Phi(\mathbf{x},\mathbf{y}) \frac{\partial u}{\partial n}(\mathbf{y}) ds(\mathbf{y}), \quad \mathbf{x} \in \mathbb{R}^3 \setminus \bar{D}, \tag{1.3}$$

where

$$\Phi(\mathbf{x},\mathbf{y}) := \frac{1}{4\pi} \frac{\exp(ik|\mathbf{x}-\mathbf{y}|)}{|\mathbf{x}-\mathbf{y}|} \tag{1.4}$$

is the fundamental solution of the Helmholtz equation and $\boldsymbol{n}(\mathbf{y})$ denotes the unit outward normal to ∂D at the point $\mathbf{y} \in \partial D$. Further, the radiating solution u has the asymptotic behaviour of an outgoing spherical wave [8, Theorem 2.5]:

$$u(\mathbf{x}) = \frac{e^{ik|\mathbf{x}|}}{|\mathbf{x}|} \left\{ u_\infty(\hat{\mathbf{x}}) + O\left(\frac{1}{|\mathbf{x}|}\right) \right\}, \tag{1.5}$$

as $|\mathbf{x}| \to \infty$ uniformly in all directions $\hat{\mathbf{x}} = \mathbf{x}/|\mathbf{x}|$. In (1.5), the function u_∞ is known as the *far field pattern* of u, and it is defined on the unit sphere (denoted throughout the paper by ∂B). Computation of the far field pattern plays an important role in inverse scattering theory, to identify the shape of the scatterers, such as buried objects [8, 9] .

If we know the radiating solution u and its normal derivative only on the surface ∂D, then a computable representation of the far field pattern u_∞ can be obtained, based on the asymptotics of the fundamental solution:

$$\Phi(\mathbf{x},\mathbf{y}) = \frac{e^{ik|\mathbf{x}|}}{4\pi|\mathbf{x}|} \left\{ e^{-ik\hat{\mathbf{x}}.\mathbf{y}} + O(\frac{1}{|\mathbf{x}|}) \right\}, \quad \frac{\partial \Phi(\mathbf{x},\mathbf{y})}{\partial n(\mathbf{y})} = \frac{e^{ik|\mathbf{x}|}}{4\pi|\mathbf{x}|} \left\{ \frac{\partial e^{-ik\hat{\mathbf{x}}.\mathbf{y}}}{\partial n(\mathbf{y})} + O(\frac{1}{|\mathbf{x}|}) \right\}. \tag{1.6}$$

Using the direct representation formula (1.3) (or other types of indirect representations [7, 8, 18]), and depending on the boundary condition, the radiating solution u and its far field pattern u_∞ can thus be computed, essentially by solving a surface integral equation.

In the next section, following [7, 8, 18], we describe boundary integral equations for solving (1.1)–(1.2) with Dirichlet, Neumann and Robin boundary conditions. We introduce tools needed for approximating these in §2.4. Our algorithm and implementation details are described §3. We give numerical results in §4. Finally the relevant stability and convergence results are presented in the Appendix.

2 Model problems and approximations

The classical boundary-value problems for the exterior Helmholtz equation are:

Exterior Dirichlet sound–soft obstacle problem

Find the radiating solution u of the Helmholtz equation (1.1) satisfying the Dirichlet boundary condition

$$u = f \qquad \text{on} \quad \partial D. \tag{2.1}$$

Exterior Robin absorbing (Neumann sound–hard) obstacle problem
Find the radiating solution u of the Helmholtz equation (1.1) satisfying the impedance (Neumann) boundary condition

$$\frac{\partial u}{\partial n} + i\mu u = g, \qquad \text{on} \quad \partial D, \quad \mu > 0 \ (\mu = 0). \tag{2.2}$$

In case of scattering of a given incoming wave u^I by a sound–soft obstacle D, the Dirichlet data f in (2.1) is given by $f = -u^I$ and the solution of (1.1)–(2.1) gives the scattered field $u = u^S$. For the absorbing (sound–hard) obstacle scattering case, the Robin (Neumann) data g in (2.2) is given by $g = -\frac{\partial u^I}{\partial n} - i\mu u^I$.

These problems have unique solutions for $k > 0$ and each of them can be reformulated as a boundary integral equation in several ways (see, e.g. [7, 8, 18]). In this paper we restrict to second-kind direct or indirect formulations, all of which are of the general form described in §2.1 - see (2.3). Although our high–order solution method can be applied to any equation of the general form (2.3), in this paper we compute only scattering examples. Examples of reformulations of the above boundary value problems into the form (2.3) is reviewed in §2.2.

2.1 General surface integral equation

In the next subsection, following [7, 8, 18], we review three distinct classes of boundary integral equations that are equivalent to the exterior problems (see (2.11), (2.13), (2.16) and (2.19)–(2.25)). These three boundary integral equations can be written as a uniquely solvable general boundary integral operator equation

$$w + \mathcal{M}w = [\alpha I + \mathcal{N}]\, h, \qquad \text{on} \quad \partial D, \tag{2.3}$$

for the unknown w and for a given function h on ∂D. Here $\mathcal{M}, \mathcal{N}$ are linear, weakly singular integral operators on ∂D, of the form

$$\mathcal{M}\psi(\mathbf{x}) = \int_{\partial D} m(\mathbf{x},\mathbf{y})\psi(\mathbf{y})ds(\mathbf{y}), \quad \mathcal{N}\psi(\mathbf{x}) = \int_{\partial D} n(\mathbf{x},\mathbf{y})\psi(\mathbf{y})ds(\mathbf{y}), \quad \mathbf{x} \in \partial D. \tag{2.4}$$

The kernel functions $m(\mathbf{x},\mathbf{y})$, $n(\mathbf{x},\mathbf{y})$ are of the form

$$m(\mathbf{x},\mathbf{y}) = \frac{1}{|\mathbf{x}-\mathbf{y}|} m_1(\mathbf{x},\mathbf{y}) + m_2(\mathbf{x},\mathbf{y}), \qquad n(\mathbf{x},\mathbf{y}) = \frac{1}{|\mathbf{x}-\mathbf{y}|} n_1(\mathbf{x},\mathbf{y}) + n_2(\mathbf{x},\mathbf{y}) \tag{2.5}$$

with m_i, for $i = 1, 2$, of the form

$$m_i(\mathbf{x},\mathbf{y}) = m_{i,1}(\mathbf{x},\mathbf{y}) + m_{i,2}(\mathbf{x},\mathbf{y})\frac{(\mathbf{x}-\mathbf{y})^T\boldsymbol{n}(\mathbf{y})}{|\mathbf{x}-\mathbf{y}|^2} + m_{i,3}(\mathbf{x},\mathbf{y})\frac{(\mathbf{x}-\mathbf{y})^T\boldsymbol{n}(\mathbf{x})}{|\mathbf{x}-\mathbf{y}|^2}\ , \tag{2.6}$$

with each $m_{i,j}$ *infinitely continuously differentiable* on $\mathbb{R}^3 \times \mathbb{R}^3$, $i = 1, 2,\ j = 1, 2, 3$. We define n_i, for $i = 1, 2$ similarly, with m in (2.6) replaced by n. In the RHS of (2.3) $\alpha \in \mathbb{R}$, and I is the identity operator.

The general operator equation (2.3) with $\mathcal{N} = 0$ was considered in [13]. However, as described in (2.16), for the Neumann sound–hard and Robin absorbing obstacle problems, we need to allow an integral operator $\mathcal{N}$, similar to that of the weakly singular operator $\mathcal{M}$.

In this paper, we introduce a practical variant of the fully discrete computational scheme of [13] for (2.3). In addition, we describe and analyse new methods to compute approximate solutions on the exterior region $\mathbb{R}^3 \setminus \bar{D}$ and the far field pattern.

Using the unique solution of w of (2.3) on the surface ∂D , solutions to the Helmholtz problems on the exterior region $\mathbb{R}^3 \setminus \bar{D}$ can be written in a unified way as

$$w(\mathbf{x}) = \int_{\partial D} \tilde{m}(\mathbf{x}, \mathbf{y}) w(\mathbf{y}) ds(\mathbf{y}) + \int_{\partial D} \tilde{n}(\mathbf{x}, \mathbf{y}) \tilde{h}(\mathbf{y}) ds(\mathbf{y}), \quad \mathbf{x} \in \mathbb{R}^3 \setminus \bar{D}, \tag{2.7}$$

where the smooth kernel function $\tilde{m}$ is defined on $(\mathbb{R}^3 \setminus \bar{D}) \times \partial D$, with representation analogous to m. For the Dirichlet problem $\tilde{n} = 0 = \tilde{h}$ and for the Neumann and Robin problems $\tilde{n} = \Phi$ and $\tilde{h} = h$. (See concrete representations (2.10), (2.14) and (2.17).) Throughout the paper $\tilde{h} = h$ or 0.

Further, the far field pattern w_∞ associated with the solution w of (2.3) gives a unified representation of the far field pattern of the Helmholtz problems (see 2.12), (2.15) and (2.18)). The general form of w_∞ is given by

$$w_\infty(\hat{\mathbf{x}}) = \int_{\partial D} m^f(\hat{\mathbf{x}}, \mathbf{y}) w(\mathbf{y}) ds(\mathbf{y}) + \int_{\partial D} n^f(\hat{\mathbf{x}}, \mathbf{y}) \tilde{h}(\mathbf{y}) ds(\mathbf{y}), \quad \hat{\mathbf{x}} \in \partial B, \tag{2.8}$$

where m^f, n^f are defined on $\partial B \times \partial D$, and are linear combinations of $e^{-ik\hat{\mathbf{x}}.\mathbf{y}}$ and $\partial e^{-ik\hat{\mathbf{x}}.\mathbf{y}}/\partial n(\mathbf{y})$.

2.2 Concrete surface integral representations

We now review various reformulations of the above exterior Helmholtz problems and show that they are all of the general form (2.3). For this we need the single- and double-layer operators:

$$\mathcal{S}\psi(\mathbf{x}) := 2 \int_{\partial D} \Phi(\mathbf{x}, \mathbf{y}) \psi(\mathbf{y}) ds(\mathbf{y}), \qquad \mathcal{K}\psi(\mathbf{x}) := 2 \int_{\partial D} \frac{\partial \Phi(\mathbf{x}, \mathbf{y})}{\partial n(\mathbf{y})} \psi(\mathbf{y}) ds(\mathbf{y}) \ , \tag{2.9}$$

for $\mathbf{x} \in \partial D$, $\psi \in C(\partial D)$, the space of all continuous functions on ∂D .

The Exterior Dirichlet Problem.
Following [8, p. 48], we can represent the solution u by

$$u(\mathbf{x}) = \int_{\partial D} \left\{ \frac{\partial \Phi(\mathbf{x}, \mathbf{y})}{\partial n(\mathbf{y})} - i\gamma \Phi(\mathbf{x}, \mathbf{y}) \right\} v(\mathbf{y}) ds(\mathbf{y}), \qquad \mathbf{x} \in \mathbb{R}^3 \setminus \bar{D}, \tag{2.10}$$

where $v \in C(\partial D)$ is found by solving:

$$v + \mathcal{K}v - i\gamma \mathcal{S}v = 2f. \tag{2.11}$$

Then, by using (1.6) in (2.10), the far field pattern is:

$$u_\infty(\hat{\mathbf{x}}) = \frac{1}{4\pi}\int_{\partial D}\left\{\frac{\partial e^{-ik\hat{\mathbf{x}}.\mathbf{y}}}{\partial n(\mathbf{y})} - i\gamma e^{-ik\hat{\mathbf{x}}.\mathbf{y}}\right\} v(\mathbf{y})ds(\mathbf{y}), \quad \hat{\mathbf{x}} \in \partial B. \tag{2.12}$$

In (2.10)–(2.12), $\gamma > 0$ is an arbitrary positive constant. It is well known that direct boundary integral formulations based on the Green's formula (1.3) for general exterior problems yield non-uniquely solvable surface integral equations for certain non-physical values of k [7, 8, 18]. Hence, we used the indirect formulation above using the combined layer potentials for the general exterior Dirichlet problem.

However, in the particular case of a direct scattering problem, with the Dirichlet boundary data f in (2.1) given by a plane wave: $f(\mathbf{x}) = -u^I(\mathbf{x}) := -e^{ik\mathbf{x}.\hat{\mathbf{d}}}$ at a fixed unit direction vector $\hat{\mathbf{d}}$, we may use the Green's formula (1.3) to obtain the exterior solution, known as the scattered field, denoted by u^S. More precisely, using the fact that the plane wave satisfies the Helmholtz equation on the whole of $\mathbb{R}^3$, and the total field $u^T(:= u^I + u^S)$ and u^S satisfy the exterior Helmholtz problem, $v := \frac{\partial u^T}{\partial n}$ satisfies the boundary integral equation [8, p. 59]

$$v + \mathcal{K}'v - i\mathcal{S}v = 2\frac{\partial u^I}{\partial n} - 2iu^I, \qquad \text{on} \quad \partial D \tag{2.13}$$

where $\mathcal{K}'$ denotes the normal derivative of $\mathcal{S}$. Using the solution v of (2.13), the scattered field u^S on the exterior region $\mathbb{R}^3 \setminus \bar{D}$, is:

$$u^S(\mathbf{x}) = -\int_{\partial D}\Phi(\mathbf{x},\mathbf{y})v(\mathbf{y})ds(\mathbf{y}), \quad \mathbf{x} \in \mathbb{R}^3 \setminus \bar{D}\ , \tag{2.14}$$

and the far field pattern of u is:

$$u_\infty(\hat{\mathbf{x}}) = -\frac{1}{4\pi}\int_{\partial D} e^{-ik\hat{\mathbf{x}}.\mathbf{y}}v(\mathbf{y})ds(\mathbf{y}) \qquad \hat{\mathbf{x}} \in \partial B. \tag{2.15}$$

The Exterior Robin(Neumann) Problem.
Letting $\mathbf{x} \to \partial D$ in (1.3), and using the jump relations of the layer potentials, we get

$$-u + \mathcal{K}u - \mathcal{S}\frac{\partial u}{\partial n} = 0 \qquad \text{on} \quad \partial D\ .$$

Substituting (2.2), we obtain the boundary integral equation:

$$u - \mathcal{K}u - i\mu\mathcal{S}u = -\mathcal{S}g \qquad \text{on} \quad \partial D, \qquad \mu > 0\ (\mu = 0). \tag{2.16}$$

Throughout this paper for the exterior Robin (Neumann) Helmholtz problem, we assume that k is not an interior Dirichlet eigenvalue. This ensures that (2.16) is uniquely solvable ([7, p.98]) and the solution of the exterior Robin (Neumann) problem is:

$$u(\mathbf{x}) = \int_{\partial D}\left[\frac{\partial\Phi(\mathbf{x},\mathbf{y})}{\partial n(\mathbf{y})}u(\mathbf{y}) + i\mu\Phi(\mathbf{x},\mathbf{y})u(\mathbf{y}) - \Phi(\mathbf{x},\mathbf{y})g(\mathbf{y})\right]ds(\mathbf{y}),\ \mathbf{x} \in \mathbb{R}^3 \setminus \bar{D} \tag{2.17}$$

and the corresponding far field pattern is:

$$u_\infty(\hat{\mathbf{x}}) = \frac{1}{4\pi}\int_{\partial D}\left[\frac{\partial e^{-ik\hat{\mathbf{x}}.\mathbf{y}}}{\partial n(\mathbf{y})}u(\mathbf{y}) + i\mu e^{-ik\hat{\mathbf{x}}.\mathbf{y}}u(\mathbf{y}) - e^{-ik\hat{\mathbf{x}}.\mathbf{y}}g(\mathbf{y})\right]ds(\mathbf{y}),\ \hat{\mathbf{x}} \in \partial B. \tag{2.18}$$

In order to put (2.11), (2.13) and (2.16) into the general form discussed in Subsection 2.1, it is necessary ([8, 22]) to split write the single- and the double-layer acoustic operators as follows:

$$\mathcal{S}\psi(\mathbf{x}) = \frac{1}{2\pi}\left[\mathcal{S}^c\psi(\mathbf{x}) + i\mathcal{S}^s\psi(\mathbf{x})\right], \qquad \mathcal{K}\psi(\mathbf{x}) = \frac{1}{2\pi}\left[\mathcal{K}^c\psi(\mathbf{x}) + i\mathcal{K}^s\psi(\mathbf{x})\right], \quad (2.19)$$

where

$$\mathcal{S}^c\psi(\mathbf{x}) := \int_{\partial D}\frac{1}{|\mathbf{x}-\mathbf{y}|}S^c(\mathbf{x},\mathbf{y})\psi(\mathbf{y})ds(\mathbf{y}); \quad \mathcal{S}^s\psi(\mathbf{x}) := \int_{\partial D} S^s(\mathbf{x},\mathbf{y})\psi(\mathbf{y})ds(\mathbf{y}), \quad (2.20)$$

$$\mathcal{K}^c\psi(\mathbf{x}) := \int_{\partial D}\frac{1}{|\mathbf{x}-\mathbf{y}|}K^c(\mathbf{x},\mathbf{y})\psi(\mathbf{y})ds(\mathbf{y}); \quad \mathcal{K}^s\psi(\mathbf{x}) := \int_{\partial D} K^s(\mathbf{x},\mathbf{y})\psi(\mathbf{y})ds(\mathbf{y}). \quad (2.21)$$

Here the kernels S^s, S^c, K^s, K^c are:

$$S^c(\mathbf{x},\mathbf{y}) := \cos(k|\mathbf{x}-\mathbf{y}|), \quad S^s(\mathbf{x},\mathbf{y}) := \begin{cases} \sin(k|\mathbf{x}-\mathbf{y}|)|\mathbf{x}-\mathbf{y}|^{-1}, & \text{if } \mathbf{x}\neq\mathbf{y} \\ k & \text{if } \mathbf{x}=\mathbf{y} \end{cases} \quad (2.22)$$

and

$$\begin{aligned} K^c(\mathbf{x},\mathbf{y}) &:= \frac{(\mathbf{x}-\mathbf{y})^T\boldsymbol{n}(\mathbf{y})}{|\mathbf{x}-\mathbf{y}|^2}S^c(\mathbf{x},\mathbf{y}) + k(\mathbf{x}-\mathbf{y})^T\boldsymbol{n}(\mathbf{y})S^s(\mathbf{x},\mathbf{y}), \\ K^s(\mathbf{x},\mathbf{y}) &:= \frac{(\mathbf{x}-\mathbf{y})^T\boldsymbol{n}(\mathbf{y})}{|\mathbf{x}-\mathbf{y}|^2}\left[S^s(\mathbf{x},\mathbf{y}) - kS^c(\mathbf{x},\mathbf{y})\right]. \end{aligned} \quad (2.23)$$

Note that the kernels S^c, S^s, K^c, K^s are infinitely continuously differentiable on $\mathbb{R}^3\times\mathbb{R}^3$.

Moreover, the normal derivative of the single layer operator should be represented as

$$\mathcal{K}'\psi(\mathbf{x}) = \frac{1}{2\pi}\left[(\mathcal{K}^c)'\psi(\mathbf{x}) - i(\mathcal{K}^s)'\psi(\mathbf{x})\right], \quad (2.24)$$

where

$$(\mathcal{K}^c)'\psi(\mathbf{x}) := \int_{\partial D}\frac{1}{|\mathbf{x}-\mathbf{y}|}K^c(\mathbf{y},\mathbf{x})\psi(\mathbf{y})ds(\mathbf{y}); \quad (\mathcal{K}^s)'\psi(\mathbf{x}) := \int_{\partial D} K^s(\mathbf{y},\mathbf{x})\psi(\mathbf{y})ds(\mathbf{y}). \quad (2.25)$$

Using (2.19)–(2.25), it is easy to see that equations (2.11), (2.13) and (2.16) are special cases of the general boundary integral equation (2.3). Further the exterior solution representations (2.10), (2.14) and (2.17) can be written in the general form (2.7) and the three far field representations (2.12), (2.15) and (2.18) are special cases of (2.8).

From now on until the end of §3, we shall describe our algorithm for discretisation of (2.3), computation of (2.7) and (2.8). In §4 we shall illustrate this general procedure on a range of particular obstacle scattering Helmholtz boundary-value problems taken from those reviewed above.

2.3 Boundary integral equation on the sphere

The main ingredient of our algorithm is the assumption that the domain D with boundary ∂D can be described globally in spherical coordinates : *Throughout the paper, we*

assume that there exists a bijective parametrisation map $\boldsymbol{q} : \partial B \to \partial D$ so that the following identity holds, for any integrable function ψ on ∂D:

$$\int_{\partial D} \psi(\mathbf{x}) ds(\mathbf{x}) = \int_{\partial B} \psi(\boldsymbol{q}(\hat{\mathbf{x}})) J(\hat{\mathbf{x}}) ds(\hat{\mathbf{x}}) \ , \tag{2.26}$$

where J is the Jacobian of $\boldsymbol{q}$. (For non–trivial examples of such smooth and non–smooth obstacles, see Figure 4.1.) We also assume that we know $\boldsymbol{q}$ and J analytically (or suitably accurate approximations to them).

Throughout this paper, we use the notation $\mathbf{x}, \mathbf{y}, \mathbf{z}$ for points on the given surface ∂D and the corresponding transformed coordinates on ∂B are denoted by $\hat{\mathbf{x}}, \hat{\mathbf{y}}, \hat{\mathbf{z}}$, and it is convenient to use spherical polar coordinates:

$$\hat{\mathbf{x}} = \boldsymbol{p}(\theta, \phi) := (\sin\theta\cos\phi, \sin\theta\sin\phi, \cos\theta)^{\mathrm{T}} \ . \tag{2.27}$$

Using the bijective parametrisation map, the surface integral equation (2.3) can be written as a equation on the unit sphere. More precisely, we have

$$w(\boldsymbol{q}(\hat{\mathbf{x}})) + \mathcal{M} w(\boldsymbol{q}(\hat{\mathbf{x}})) = [\alpha I + \mathcal{N}]\, h(\boldsymbol{q}(\hat{\mathbf{x}})) \qquad \hat{\mathbf{x}} \in \partial B. \tag{2.28}$$

Now, defining

$$W(\hat{\mathbf{x}}) = w(\boldsymbol{q}(\hat{\mathbf{x}})), \quad H(\hat{\mathbf{x}}) = h(\boldsymbol{q}(\hat{\mathbf{x}})), \quad \hat{\mathbf{x}} \in \partial B, \tag{2.29}$$

we can rewrite (2.28) as

$$W(\hat{\mathbf{x}}) + \mathcal{M} W(\hat{\mathbf{x}}) = [\alpha I + \mathcal{N}]\, H(\hat{\mathbf{x}}) \qquad \hat{\mathbf{x}} \in \partial B. \tag{2.30}$$

Here (and in rest of the paper), the combined layer operators $\mathcal{M}$, $\mathcal{N}$ are integral operators on the unit sphere, with following details: For a given $\Psi \in L^2(\partial B)$, and $\hat{\mathbf{x}} \in \partial B$, using (2.4)–(2.5),

$$\mathcal{M}\Psi(\hat{\mathbf{x}}) := [\mathcal{M}_1 + \mathcal{M}_2]\, \Psi(\hat{\mathbf{x}}), \qquad \mathcal{N}\Psi(\hat{\mathbf{x}}) := [\mathcal{N}_1 + \mathcal{N}_2]\, \Psi(\hat{\mathbf{x}}), \tag{2.31}$$

with

$$\mathcal{M}_1\Psi(\hat{\mathbf{x}}) := \int_{\partial B} \frac{1}{|\hat{\mathbf{x}} - \hat{\mathbf{y}}|} M_1(\hat{\mathbf{x}}, \hat{\mathbf{y}}) \Psi(\hat{\mathbf{y}}) ds(\hat{\mathbf{y}}); \quad \mathcal{M}_2\psi(\mathbf{x}) := \int_{\partial B} M_2(\hat{\mathbf{x}}, \hat{\mathbf{y}}) \Psi(\hat{\mathbf{y}}) ds(\hat{\mathbf{y}}), \tag{2.32}$$

$$\mathcal{N}_1\Psi(\hat{\mathbf{x}}) := \int_{\partial B} \frac{1}{|\hat{\mathbf{x}} - \hat{\mathbf{y}}|} N_1(\hat{\mathbf{x}}, \hat{\mathbf{y}}) \Psi(\hat{\mathbf{y}}) ds(\hat{\mathbf{y}}); \quad \mathcal{N}_2\Psi(\hat{\mathbf{x}}) := \int_{\partial B} N_2(\hat{\mathbf{x}}, \hat{\mathbf{y}}) \Psi(\hat{\mathbf{y}}) ds(\hat{\mathbf{y}}), \tag{2.33}$$

where using the representative kernel

$$R(\hat{\mathbf{x}}, \hat{\mathbf{y}}) := \frac{|\hat{\mathbf{x}} - \hat{\mathbf{y}}|}{|\boldsymbol{q}(\hat{\mathbf{x}}) - \boldsymbol{q}(\hat{\mathbf{y}})|} \ , \tag{2.34}$$

the kernels M_1, M_2, N_1, N_2 on $\partial B \times \partial B$ are given by

$$M_1(\hat{\mathbf{x}}, \hat{\mathbf{y}}) := R(\hat{\mathbf{x}}, \hat{\mathbf{y}}) m_1(\boldsymbol{q}(\hat{\mathbf{x}}), \boldsymbol{q}(\hat{\mathbf{y}})) J(\hat{\mathbf{y}}), \quad M_2(\hat{\mathbf{x}}, \hat{\mathbf{y}}) := m_2(\boldsymbol{q}(\hat{\mathbf{x}}), \boldsymbol{q}(\hat{\mathbf{y}})) J(\hat{\mathbf{y}}), \tag{2.35}$$

$$N_1(\hat{\mathbf{x}}, \hat{\mathbf{y}}) := R(\hat{\mathbf{x}}, \hat{\mathbf{y}}) n_1(\boldsymbol{q}(\hat{\mathbf{x}}), \boldsymbol{q}(\hat{\mathbf{y}})) J(\hat{\mathbf{y}}), \quad N_2(\hat{\mathbf{x}}, \hat{\mathbf{y}}) := n_2(\boldsymbol{q}(\hat{\mathbf{x}}), \boldsymbol{q}(\hat{\mathbf{y}})) J(\hat{\mathbf{y}}). \tag{2.36}$$

2.4 Discrete spectral projection

We shall approximate the equation (2.30) in the $(n+1)^2$-dimensional space of all spherical polynomials of degree $\leq n$, which we denote $\mathbb{P}_n$. A convenient orthonormal basis for $\mathbb{P}_n$ is the spherical harmonics:

$$Y_{l,j}(\hat{\mathbf{x}}) = (-1)^{(j+|j|)/2}\sqrt{\frac{2l+1}{4\pi}\frac{(l-|j|)!}{(l+|j|)!}}\;\; P_l^{|j|}(\cos\theta)\,\exp(ij\phi), \quad 0 \leq l \leq n, \quad |j| \leq l, \tag{2.37}$$

where we used the coordinates (2.27) and $P_l^{|j|}$ are the associated Legendre functions.

Central to our algorithm is the fact that the spherical harmonics are eigenfunctions of the single layer potential operator on the sphere [8]:

$$\int_{\partial B} \frac{1}{|\hat{\mathbf{x}}-\hat{\mathbf{y}}|} Y_{l,j}(\hat{\mathbf{y}})ds(\hat{\mathbf{y}}) = \frac{4\pi}{2l+1} Y_{l,j}(\hat{\mathbf{x}}) \;, \quad \hat{\mathbf{x}} \in \partial B. \tag{2.38}$$

The standard *Galerkin method* for (2.30) seeks an approximate solution $W_n \in \mathbb{P}_n$, satisfying

$$(W_n, \Phi_n) + (\mathcal{M}W_n, \Phi_n) = ([\alpha I + \mathcal{N}]\, H, \Phi_n)\,, \quad \text{for all} \;\; \Phi_n \in \mathbb{P}_n, \tag{2.39}$$

with $(\cdot,\cdot)$ denoting the usual inner product on ∂B. In practice, we have to approximate this using cubature rules on ∂B of the form:

$$\int_{\partial B} \Psi(\hat{\mathbf{x}})ds(\hat{\mathbf{x}}) \cong \sum_{j=1}^{m} \zeta_j \Psi(\hat{\mathbf{x}}_j) =: Q_m\Psi, \quad \Psi \in C(\partial B). \tag{2.40}$$

From (2.40) we build a discrete version of the inner product on ∂B:

$$(\Psi_1, \Psi_2)_m := Q_m(\Psi_1\Psi_2) = \sum_{j=1}^{m} \zeta_j \Psi_1(\hat{\mathbf{x}}_j)\overline{\Psi_2(\hat{\mathbf{x}}_j)}\;, \quad \Psi_1, \Psi_2 \in C(\partial B). \tag{2.41}$$

In this paper we shall restrict to the specific $2(n+1)\times(n+1)-$point rectangle-Gauss rule, given by:

$$\int_{\partial B} \Psi(\hat{\mathbf{x}})ds(\hat{\mathbf{x}}) \cong \sum_{r=0}^{2n+1}\sum_{s=1}^{n+1} \mu_r\nu_s \Psi(\boldsymbol{p}(\theta_s,\phi_r)), \tag{2.42}$$

with $\boldsymbol{p}(\theta,\phi)$ defined as in (2.27), $\theta_s = \cos^{-1} z_s$, where $z_s,\ s = 1,\ldots,n+1$, are the zeros of the Legendre polynomial of degree $n+1$, and $\nu_s,\ s = 1,\ldots,n+1$, are the corresponding Gauss-Legendre weights and

$$\mu_r = \frac{\pi}{n+1}, \quad \phi_r = \frac{r\pi}{n+1}, \quad r = 0,\ldots,2n+1\;. \tag{2.43}$$

The number of quadrature points $m = 2(n+1)^2$ in the above rule is twice the dimension of the approximation space $\mathbb{P}_n$. Other "tensor-product" rules are also possible, see the discussion in [13] and references therein. The rule (2.40) is exact for spherical polynomials of degree $2n$.

Corresponding to the discrete inner product (2.41), we have also a discrete orthogonal projection operator $\mathcal{L}_n : C(\partial B) \to \mathbb{P}_n$, defined by

$$\mathcal{L}_n\Psi \;=\; \sum_{l=0}^{n}\sum_{|j|\leq l} (\Psi, Y_{l,j})_m Y_{l,j}, \qquad\qquad \Psi \in C(\partial B). \tag{2.44}$$

The *hyperinterpolation* operator $\mathcal{L}_n$ satisfies $\mathcal{L}_n\Phi_n = \Phi_n$, for any $\Phi_n \in \mathbb{P}_n$ [19].

3 Fully discrete spectral approximations

Following [13], and with the help of the above cubature and the hyperinterpolation procedures, we first introduce approximations to the integral operators (2.31) in the space $\mathbb{P}_n$.

3.1 Discrete integral operators

The operators $\mathcal{M}$ and $\mathcal{N}$ defined in (2.31)–(2.36) contain weakly singular components $\mathcal{M}_1$ and $\mathcal{N}_1$ and smooth components $\mathcal{M}_2$ and $\mathcal{N}_2$. We approximate these in different ways.

Weakly singular components

To deal with the weak singularity in $\mathcal{M}_1, \mathcal{N}_1$, we introduce a change of coordinate system on ∂B, that will yield transformed operators with kernels which are singular only at one point on the sphere, namely the north pole. To this end, for each $\hat{\mathbf{x}} \in \partial B$, we introduce a 3×3 orthogonal matrix $T_{\hat{\mathbf{x}}}$ which carries $\hat{\mathbf{x}}$ to the north pole: $T_{\hat{\mathbf{x}}}\hat{\mathbf{x}} = (0, 0, 1)^T = \hat{\mathbf{n}}$. If $\hat{\mathbf{x}} = \boldsymbol{p}(\theta, \phi)$, then an explicit form of $T_{\hat{\mathbf{x}}}$ is

$$T_{\hat{\mathbf{x}}} := P(\phi)Q(-\theta)P(-\phi), \tag{3.1}$$

where $P(\psi)$ and $Q(\psi)$ are 3×3 matrices corresponding to positive rotations by ψ about the $z-$ axis and $y-$axis respectively,

$$P(\psi) := \begin{pmatrix} \cos\psi & -\sin\psi & 0 \\ \sin\psi & \cos\psi & 0 \\ 0 & 0 & 1 \end{pmatrix}, \qquad Q(\psi) := \begin{pmatrix} \cos\psi & 0 & \sin\psi \\ 0 & 1 & 0 \\ -\sin\psi & 0 & \cos\psi \end{pmatrix}. \tag{3.2}$$

The matrix $T_{\hat{\mathbf{x}}}$ is then continuous in $\hat{\mathbf{x}}$. At this point, it is useful to introduce an induced linear transformation $\mathcal{T}_{\hat{\mathbf{x}}}$ on $C(\partial B)$ as

$$\mathcal{T}_{\hat{\mathbf{x}}}\Psi(\hat{\mathbf{z}}) = \Psi(T_{\hat{\mathbf{x}}}^{-1}\hat{\mathbf{z}}), \qquad \hat{\mathbf{z}} \in \partial B, \qquad \Psi \in C(\partial B). \tag{3.3}$$

For coordinate transformation of the kernels in (2.34)–(2.36), it is convenient to introduce a bivariate analogue of (3.3), also denoted $\mathcal{T}_{\hat{\mathbf{x}}}$:

$$\mathcal{T}_{\hat{\mathbf{x}}}\Psi(\hat{\mathbf{z}}_1, \hat{\mathbf{z}}_2) = \Psi(T_{\hat{\mathbf{x}}}^{-1}\hat{\mathbf{z}}_1, T_{\hat{\mathbf{x}}}^{-1}\hat{\mathbf{z}}_2), \quad \hat{\mathbf{z}}_1, \hat{\mathbf{z}}_2 \in \partial B \ , \quad \Psi \in C(\partial B \times \partial B). \tag{3.4}$$

For $\hat{\mathbf{x}}, \hat{\mathbf{z}} \in \partial B$, if we write $\hat{\mathbf{y}} = T_{\hat{\mathbf{x}}}^{-1}\hat{\mathbf{z}}$, the orthogonality of $T_{\hat{\mathbf{x}}}$ yields a useful identity

$$|\hat{\mathbf{x}} - \hat{\mathbf{y}}| = \left|T_{\hat{\mathbf{x}}}^{-1}(\hat{\mathbf{n}} - \hat{\mathbf{z}})\right| = |\hat{\mathbf{n}} - \hat{\mathbf{z}}|\,. \tag{3.5}$$

We shall describe our approximation in detail only for the operator $\mathcal{M}_1$; the procedure for $\mathcal{N}_1$ is analogous. Using (3.3), (3.4) and (3.5) and the fact that surface measure on ∂B is invariant under orthogonal transformations, we can write $\mathcal{M}_1$ as

$$\mathcal{M}_1\Psi(\hat{\mathbf{x}}) = \int_{\partial B} \frac{1}{|\hat{\mathbf{n}} - \hat{\mathbf{z}}|}\mathcal{T}_{\hat{\mathbf{x}}}M_1(\hat{\mathbf{n}}, \hat{\mathbf{z}})\mathcal{T}_{\hat{\mathbf{x}}}\Psi(\hat{\mathbf{z}})ds(\hat{\mathbf{z}}), \qquad \Psi \in C(\partial B). \tag{3.6}$$

There are two important gains from using the rotated coordinate system in (3.6). One is that, if we now rewrite $\mathcal{M}_1$ using spherical polar coordinates, then it turns out not

to have a singularity at all: for all $\hat{\mathbf{z}} = \boldsymbol{p}(\theta,\phi) \in \partial B$, the quantity $|\hat{\mathbf{n}} - \hat{\mathbf{z}}| = 2\sin(\theta/2)$ is cancelled out by the surface element $ds(\hat{\mathbf{z}}) = \sin\theta d\theta d\phi$. Furthermore, it can be shown that [13, Lemma 4.6] the map $(\theta,\phi) \to \mathcal{T}_{\hat{\mathbf{x}}} M_1(\hat{\mathbf{n}}, \boldsymbol{p}(\theta,\phi))$ is smooth.

The latter observation suggests that it may be reasonable to approximate the term $\mathcal{T}_{\hat{\mathbf{x}}} M_1(\hat{\mathbf{n}},\hat{\mathbf{z}})\mathcal{T}_{\hat{\mathbf{x}}}\Psi(\hat{\mathbf{z}})$ in (3.6) using a hyperinterpolation operator of the type defined in (2.44). Let $\mathcal{L}_{n'}$ be this hyperinterpolation operator, defined through a discrete inner product $(\Psi_1,\Psi_2)_{m'} := Q'_{m'}(\Psi_1\Psi_2)$, where, analogously to (2.40), $Q'_{m'}$ is a rule with points and weights $\hat{\mathbf{z}}_{q'}$, and $\eta_{q'}$, for $q' = 1,\cdots,m'$, i.e.

$$Q'_{m'}\Psi = \sum_{q'=1}^{m'} \eta_{q'}\Psi(\hat{\mathbf{z}}_{q'}) \ .$$

We assume this rule is exact for spherical polynomials of degree $2n'$. Our approximation $\mathcal{M}_{1,n'}$ to $\mathcal{M}_1$ in (3.6) is then defined as

$$\mathcal{M}_{1,n'}\Psi(\hat{\mathbf{x}}) := \int_{\partial B} \frac{1}{|\hat{\mathbf{n}} - \hat{\mathbf{z}}|} \mathcal{L}_{n'}\left\{\mathcal{T}_{\hat{\mathbf{x}}} M_1(\hat{\mathbf{n}},\cdot)\mathcal{T}_{\hat{\mathbf{x}}}\Psi(\cdot)\right\}(\hat{\mathbf{z}}) ds(\hat{\mathbf{z}}) \tag{3.7}$$

$$= \sum_{l=0}^{n'} \sum_{|j|\le l} \frac{4\pi}{2l+1} \left(\mathcal{T}_{\hat{\mathbf{x}}} M_1(\hat{\mathbf{n}},\cdot)\mathcal{T}_{\hat{\mathbf{x}}}\Psi(\cdot), Y_{l,j}(\cdot)\right)_{m'} Y_{l,j}(\hat{\mathbf{n}}), \tag{3.8}$$

where we used (2.44) (with n replaced by n' and m replaced by m') and (2.38). More specifically,

$$\mathcal{M}_{1,n'}\Psi(\hat{\mathbf{x}}) = \sum_{l=0}^{n'} \sum_{|j|\le l} \sum_{q'=1}^{m'} \frac{4\pi}{2l+1} \eta_{q'} \mathcal{T}_{\hat{\mathbf{x}}} M_1(\hat{\mathbf{n}},\hat{\mathbf{z}}_{q'})\mathcal{T}_{\hat{\mathbf{x}}}\Psi(\hat{\mathbf{z}}_{q'})\overline{Y_{l,j}(\hat{\mathbf{z}}_{q'})} Y_{l,j}(\hat{\mathbf{n}}). \tag{3.9}$$

Using the addition theorem for spherical harmonics [8], the representation for $\mathcal{M}_{1,n'}$ in (3.9) can be simplified as

$$\mathcal{M}_{1,n'}\Psi(\hat{\mathbf{x}}) = \sum_{q'=1}^{m'} \eta_{q'} \alpha_{q'}^{n'} \mathcal{T}_{\hat{\mathbf{x}}} M_1(\hat{\mathbf{n}},\hat{\mathbf{z}}_{q'})\mathcal{T}_{\hat{\mathbf{x}}}\Psi(\hat{\mathbf{z}}_{q'}), \qquad \Psi \in C(\partial B), \tag{3.10}$$

where $\alpha_{q'}^{n'} := \sum_{l=0}^{n'} P_l(\hat{\mathbf{n}}\cdot\hat{\mathbf{z}}_{q'})$. We note that for the (superalgebraic) convergence of $\mathcal{M}_{1,n'}$ to $\mathcal{M}_1$ it is important to choose $n' > n$ (see Appendix and [13]). For rest of the paper, we assume: *n' is dependent on n and $n'(n) > n$.* (For our computations, we took $n' = 2n$.)

Similarly, we approximate $\mathcal{N}_1$ in (2.33) by

$$\mathcal{N}_{1,n'}\Psi(\hat{\mathbf{x}}) := \sum_{q'=1}^{m'} \eta_{q'} \alpha_{q'}^{n'} \mathcal{T}_{\hat{\mathbf{x}}} N_1(\hat{\mathbf{n}},\hat{\mathbf{z}}_{q'})\mathcal{T}_{\hat{\mathbf{x}}}\Psi(\hat{\mathbf{z}}_{q'}), \qquad \Psi \in C(\partial B), \tag{3.11}$$

Smooth components

To approximate $\mathcal{M}_2, \mathcal{N}_2$ in (2.32)–(2.33), we write

$$\mathcal{M}_2\Psi(\hat{\mathbf{x}}) = \int_{\partial B} \mathcal{T}_{\hat{\mathbf{x}}} M_2(\hat{\mathbf{n}},\hat{\mathbf{z}})\mathcal{T}_{\hat{\mathbf{x}}}\Psi(\hat{\mathbf{z}}) ds(\hat{\mathbf{z}}), \qquad \Psi \in C(\partial B),$$

and define an approximation $\mathcal{M}_{2,n'}$ for $\mathcal{M}_2$ as

$$\mathcal{M}_{2,n'}\Psi(\hat{\mathbf{x}}) := \int_{\partial B} \mathcal{L}_{n'}\left\{\mathcal{T}_{\hat{\mathbf{x}}} M_2(\hat{\mathbf{n}},\cdot)\mathcal{T}_{\hat{\mathbf{x}}}\Psi(\cdot)\right\}(\hat{\mathbf{z}})ds(\hat{\mathbf{z}}), \qquad \Psi \in C(\partial B).$$

Using the definition of $\mathcal{L}_{n'}$ and the orthonormality of the spherical harmonics,

$$\mathcal{M}_{2,n'}\Psi(\hat{\mathbf{x}}) = \left(\mathcal{T}_{\hat{\mathbf{x}}} M_2(\hat{\mathbf{n}},\cdot)\mathcal{T}_{\hat{\mathbf{x}}}\Psi(\cdot),1\right)_{m'} = \sum_{q'=1}^{m'} \eta_{q'}\mathcal{T}_{\hat{\mathbf{x}}} M_2(\hat{\mathbf{n}},\hat{\mathbf{z}}_{q'})\mathcal{T}_{\hat{\mathbf{x}}}\Psi(\hat{\mathbf{z}}_{q'}). \tag{3.12}$$

Similarly, we define

$$\mathcal{N}_{2,n'}\Psi(\hat{\mathbf{x}}) := \sum_{q'=1}^{m'} \eta_{q'}\mathcal{T}_{\hat{\mathbf{x}}} N_2(\hat{\mathbf{n}},\hat{\mathbf{z}}_{q'})\mathcal{T}_{\hat{\mathbf{x}}}\Psi(\hat{\mathbf{z}}_{q'}), \qquad \Psi \in C(\partial B). \tag{3.13}$$

Combining (3.10)–(3.13), we obtain the approximations to $\mathcal{M},\mathcal{N}$:

$$\mathcal{M}_{n'}\Psi(\hat{\mathbf{x}}) := \left[\mathcal{M}_{1,n'} + \mathcal{M}_{2,n'}\right]\Psi(\hat{\mathbf{x}}), \qquad \mathcal{N}_{n'}\Psi(\hat{\mathbf{x}}) := \left[\mathcal{N}_{1,n'} + \mathcal{N}_{2,n'}\right]\Psi(\hat{\mathbf{x}}). \tag{3.14}$$

3.2 Fully discrete approximations on the surface

Using the discrete operators in (3.14), our fully discrete scheme for (2.30), written in operator form, is: find $W_n \in \mathbb{P}_n$ such that

$$W_n + \mathcal{L}_n\mathcal{M}_{n'}W_n = \left[\alpha\mathcal{L}_n + \mathcal{L}_n\mathcal{N}_{n'}\mathcal{L}_n\right]H. \tag{3.15}$$

To implement this we set

$$W_n = \sum_{l=0}^{n}\sum_{|j|\le l} \omega_{lj}Y_{l,j}, \tag{3.16}$$

and compute the coefficients ω_{lj} by solving the system:

$$\begin{aligned}(W_n, Y_{l',j'})_m + (\mathcal{M}_{n'}W_n, Y_{l',j'})_m &= \alpha(H,Y_{l',j'})_m + \sum_{l=0}^{n}\sum_{|j|\le l}(\mathcal{N}_{n'}Y_{l,j},Y_{l',j'})_m(H,Y_{l,j})_m,\\ &\qquad \text{for } \; l' = 0,\ldots,n,\ |j'| \le l'. \end{aligned} \tag{3.17}$$

Note that, written this way, our algorithm looks like a discrete Galerkin method. However, it is shown in [13] that, after a simple transformation, it can also be written as a variant of the Nyström method of Wienert (see [22], [8, p.83]), to be solved for a slightly different dependent variable. The reason we do not use the Nyström formulation is that in this case the corresponding linear system has a dimension about twice that of the discrete Galerkin system considered here (see [13]).

Inserting (3.16) into (3.17) we see that $\boldsymbol{\omega} := (\omega_{lj})$ solves:

$$\left[\mathbf{I} + \mathbf{M}\right]\boldsymbol{\omega} = \left[\alpha\mathbf{I} + \mathbf{N}\right]\mathbf{h}, \tag{3.18}$$

where for $l,l' = 0,\ldots,n, |j| \le l, |j'| \le l'$ the $l'j', lj$ entry of the matrices and the $l'j'-$th component of $\mathbf{h}$ are given by

$$\begin{aligned} \mathbf{M}_{l'j',lj} &= (\mathcal{M}_{n'}Y_{l,j},Y_{l',j'})_m; & \mathbf{I}_{l'j',lj} &= \delta_{l'l}\delta_{j'j},\\ \mathbf{N}_{l'j',lj} &= (\mathcal{N}_{n'}Y_{l,j},Y_{l',j'})_m; & \mathbf{h}_{l'j'} &= (H,Y_{l',j'})_m. \end{aligned} \tag{3.19}$$

This scheme is a more practical variant of the one proposed in [13], where the approximation of the RHS layer operator in (2.30) was omitted. Here we use the fact that when H is smooth, it will be sufficient to approximate it to the same accuracy as we expect for the solution of (2.30).

We compute the corresponding approximation of the solution w of (2.3) by setting

$$w_n(\mathbf{x}) := W_n(\hat{\mathbf{x}}), \qquad \mathbf{x} = \boldsymbol{q}(\hat{\mathbf{x}}) \in \partial D. \tag{3.20}$$

In the Appendix, Theorem A.1, we prove that w_n converges superalgebraically to w. More precisely, if the given data is smooth, then for any $r > 0$, the maximum error on ∂D, denoted by $\|w - w_n\|_{\infty,\partial D}$, is of order $O\left(n^{-r}\right)$.

3.3 Implementation

To complete the practical description of the first part of our algorithm to compute the density W_n of the combined approximate single–double layer acoustic operators, all that remains is to describe the efficient computation of the d^2 entries of the $d \times d$ layer matrices $\mathbf{M},\ \mathbf{N}$, given by (3.19), where $d = (n+1)^2$. We show that these matrices can be set up in $O(d^{2.5})$ operations, even without using any fast transforms. As mentioned in §1, in the main and most expensive part of the algorithm associated with rotated harmonics, we describe below an efficient stable practical approach, different from the ideas given in [13, 22].

It is sufficient to describe the details for the matrix $\mathbf{M}$. Recall from (3.19), (2.41), (3.14), (3.10), and (3.12) that for $l, l' = 0, \ldots, n,\ |j| \le l,\ |j'| \le l'$, we have

$$\mathbf{M}_{l'j',lj} = \sum_{q=1}^{m} \zeta_q \sum_{q'=1}^{m'} \eta_{q'} \left[\alpha_{q'}^{n'} \mathcal{T}_{\hat{\mathbf{x}}_q} M_1(\hat{\mathbf{n}}, \hat{\mathbf{z}}_{q'}) + \mathcal{T}_{\hat{\mathbf{x}}_q} M_2(\hat{\mathbf{n}}, \hat{\mathbf{z}}_{q'})\right] \mathcal{T}_{\hat{\mathbf{x}}_q} Y_{l,j}(\hat{\mathbf{z}}_{q'}) \overline{Y_{l',j'}(\hat{\mathbf{x}}_q)}. \tag{3.21}$$

Each entry of the $d \times d$ matrix $\mathbf{M}$ consists of the approximation of a double integral over the surface ∂B and each integral over ∂B uses function evaluations at $O(d)$ points, so the complexity of assembly of $\mathbf{M}$ is potentially $O(d^4) = O(n^8)$. We device an efficient assembly algorithm which reduces this to $O(d^{2.5}) = O(n^5)$. (Note that $O(n^4)$ would be optimal complexity for the matrix assembly. We are willing to tolerate this complexity growth since the method is superalgebraically convergent.)

Recalling that the quadrature rules on the sphere which we use are defined using points of latitude and longitude (2.42), we write

$$\begin{aligned}
(\Psi_1, \Psi_2)_m &= \sum_{r=0}^{2n+1} \sum_{s=1}^{n+1} \mu_r \nu_s \Psi_1(\boldsymbol{p}(\theta_s, \phi_r)) \overline{\Psi_2(\boldsymbol{p}(\theta_s, \phi_r))}, \\
(\Psi_1, \Psi_2)_{m'} &= \sum_{r'=0}^{2n'+1} \sum_{s'=1}^{n'+1} \xi_{r'} \eta_{s'} \Psi_1(\boldsymbol{p}(\Theta_{s'}, \Phi_{r'})) \overline{\Psi_2(\boldsymbol{p}(\Theta_{s'}, \Phi_{r'}))}
\end{aligned}$$

and hence we can rewrite (3.21) as

$$\begin{aligned}
\mathbf{M}_{l'j',lj} = \sum_{r=0}^{2n+1} \sum_{s=1}^{n+1} \mu_r \nu_s \sum_{r'=0}^{2n'+1} \sum_{s'=1}^{n'+1} \xi_{r'} \eta_{s'} \Big[& \alpha_{s'}^{n'} \mathcal{T}_{\boldsymbol{p}(\theta_s,\phi_r)} M_1(\hat{\mathbf{n}}, \boldsymbol{p}(\Theta_{s'}, \Phi_{r'})) \\
& + \mathcal{T}_{\boldsymbol{p}(\theta_s,\phi_r)} M_2(\hat{\mathbf{n}}, \boldsymbol{p}(\Theta_{s'}, \Phi_{r'}))\Big] \mathcal{T}_{\boldsymbol{p}(\theta_s,\phi_r)} Y_{l,j}(\boldsymbol{p}(\Theta_{s'}, \Phi_{r'})) \overline{Y_{l',j'}(\boldsymbol{p}(\theta_s, \phi_r))},
\end{aligned} \tag{3.22}$$

where $\alpha_{s'}^{n'} = \sum_{l=0}^{n'} P_l(\cos\Theta_{s'})$.

Since the approximation space $\mathbb{P}_n$ is invariant under rotations, the rotated spherical harmonic $\mathcal{T}_{\boldsymbol{p}(\theta_s,\phi_r)}Y_{l,j}$ can be written as a linear combination of spherical harmonics of degree l. However, the efficient and stable computation of the associated Fourier coefficient matrices in this expansion (for all $l = 0, \cdots, n,\ |j| \le l,\ r = 0, \cdots, 2n+1,\ s = 1, \cdots, n+1$) is required.

As in (3.3), for a given orthogonal matrix Ω, we denote the induced linear transformation by $\mathcal{T}(\Omega)$, i.e. $\mathcal{T}(\Omega)\Psi(\hat{\mathbf{z}}) = \Psi(\Omega^{-1}\hat{\mathbf{z}})$. Using (3.1) and (3.2), we have

$$\mathcal{T}_{\boldsymbol{p}(\theta_s,\phi_r)} = \mathcal{T}(P(\phi_r))\mathcal{T}(Q(-\theta_s))\mathcal{T}(P(-\phi_r)). \tag{3.23}$$

It is easy to check that positive rotation of $Y_{l,j}(\theta,\phi)$ by an angle β about the $z-$axis (see (3.2)) yields $Y_{l,j}(\theta,\phi-\beta)$, equivalently

$$\mathcal{T}(P(\beta))Y_{l,j} = e^{-ij\beta}Y_{l,j}. \tag{3.24}$$

However, the representation of the rotated spherical harmonics about the $y-$axis is not so simple as in (3.24). Using the fact that the result of rotating $Y_{l,j}$ is also a spherical harmonic of the same degree (l), we can certainly write:

$$\mathcal{T}(Q(\alpha))Y_{l,j} = \sum_{|\tilde{j}|\le l} d_{\tilde{j}j}^{(l)}(\alpha)Y_{l,\tilde{j}}, \tag{3.25}$$

where $d^{(l)}(\alpha)$ is the required $(2l+1)\times(2l+1)$ Fourier coefficient matrix. A possible representation of this (see [2, p.22], [13]) is

$$d^{(l)}(\alpha)_{\tilde{j}j} = \sum_t (-1)^t \frac{[(l+\tilde{j})!(l-\tilde{j})!(l+j)!(l-j)!]^{1/2}}{(l+\tilde{j}-t)!(l-j-t)!t!(t+j-\tilde{j})!}\left(\cos\frac{\alpha}{2}\right)^{2l+\tilde{j}-j-2t}\left(\sin\frac{\alpha}{2}\right)^{2t+j-\tilde{j}}, \tag{3.26}$$

with the sum over all $t = 0, 1, \cdots$ for which the arguments of the factorials are non–negative. Further, we have the following symmetry properties [2, p.147]

$$d_{\tilde{j}j}^{(l)}(\alpha) = (-1)^{\tilde{j}-j}d_{j\tilde{j}}^{(l)}(\alpha) = d_{-j-\tilde{j}}^{(l)}(\alpha) = d_{j\tilde{j}}^{(l)}(-\alpha). \tag{3.27}$$

We found that computation of $d^{(l)}$ using the formula (3.26) for higher degree harmonics (over 25) lead to a marked reduction in the accuracy of the computed solution, due to the subtraction error arising from the fact that (3.26) contains many terms of similar magnitude but with alternating signs. To find an efficient and stable formula for representing $\mathcal{T}_{p(\theta_s,\phi_r)}Y_{l,j}$ as a linear combination of spherical harmonics which both exploits the simple formula (3.24) but avoids the difficulties associated with (3.25) and (3.26), we proceed as follows.

Using (3.2) we rewrite $Q(-\theta_s)$ as

$$Q(-\theta_s) = P(\pi/2)Q(\pi/2)P(-\theta_s)Q(-\pi/2)P(-\pi/2). \tag{3.28}$$

Hence from (3.23), with $\Gamma_Z^{\pm} = \mathcal{T}(P(\pm\pi/2))$ and $\Gamma_Y^{\pm} = \mathcal{T}(Q(\pm\pi/2))$, we get

$$\mathcal{T}_{\boldsymbol{p}(\theta_s,\phi_r)} = \mathcal{T}(P(\phi_r))\ \Gamma_Z^+\ \Gamma_Y^+\ \mathcal{T}(P(-\theta_s))\ \Gamma_Y^-\ \Gamma_Z^-\ \mathcal{T}(P(-\phi_r)). \tag{3.29}$$

Using (3.24), (3.25), (3.29) and the fact that $d^{(l)}_{\tilde{j}j}(\pi/2) = d^{(l)}_{j\tilde{j}}(-\pi/2)$ (see (3.27)), it can be shown that

$$\mathcal{T}_{\boldsymbol{p}(\theta_s,\phi_r)} Y_{l,j} = \sum_{|\tilde{j}|\le l} F_{sl\tilde{j}j} e^{i(j-\tilde{j})\phi_r} Y_{l,\tilde{j}}, \tag{3.30}$$

where

$$F_{sl\tilde{j}j} = e^{i(j-\tilde{j})\pi/2} \sum_{|m|\le l} d^{(l)}_{\tilde{j}m}(\pi/2) d^{(l)}_{jm}(\pi/2) e^{im\theta_s}. \tag{3.31}$$

In order to compute the $(2l+1)\times(2l+1)$ matrix F_{sl}, we observe from (3.26) that

$$\begin{aligned} d^{(l)}_{\tilde{j}j}(\pi/2) &= 2^{-l}\left[\frac{(l+\tilde{j})!(l-\tilde{j})!}{(l+j)!(l-j)!}\right]^{1/2} \sum_{t=0}^{l+\tilde{j}} (-1)^t \begin{pmatrix} l+j \\ l+\tilde{j}-t \end{pmatrix} \begin{pmatrix} l-j \\ t \end{pmatrix} \\ &= 2^{\tilde{j}}\left[\frac{(l+\tilde{j})!(l-\tilde{j})!}{(l+j)!(l-j)!}\right]^{1/2} P^{(j-\tilde{j},-j-\tilde{j})}_{l+\tilde{j}}(0), \end{aligned} \tag{3.32}$$

where for given $q\ (= l+\tilde{j} \ge 0)$ and non-negative integers $a\ (= j-\tilde{j}),\ b\ (= -j-\tilde{j})$, $P^{(a,b)}_q(0)$ is the normalized Jacobi polynomial evaluated at zero [21, p.68]:

$$P^{(a,b)}_q(0) = 2^{-q} \sum_{t=0}^{q} (-1)^t \begin{pmatrix} q+a \\ q-t \end{pmatrix} \begin{pmatrix} q+b \\ t \end{pmatrix}. \tag{3.33}$$

For $j-\tilde{j} < 0$ or $-j-\tilde{j} < 0$, we can compute $d^{(l)}(\pi/2)_{\tilde{j}j}$ using the symmetry relation (3.27) together with the identity (3.32) for the case $\tilde{j} \le 0,\ |j| \le -\tilde{j}$. Note that the final formula (3.32) for $d^{(l)}_{\tilde{j},j}(\phi/2)$ now contains no possibility of subtraction error.

If we denote $\hat{\mathbf{x}}_{rs} = \boldsymbol{p}(\theta_s\phi_r),\ \hat{\mathbf{y}}^{r',s'}_{rs} = T^{-1}_{\boldsymbol{p}(\theta_s,\phi_r)} \boldsymbol{p}(\Theta_{s'}, \Phi_{r'})$ and the normalized coefficient of $Y_{l,j}$ in (2.37) by c^j_l, using (3.24) and (2.37) in (3.22), we get

$$\begin{aligned} \mathbf{M}_{l'j',lj} = &\sum_{r=0}^{2n+1}\sum_{s=1}^{n+1} \mu_r\nu_s \sum_{r'=0}^{2n'+1}\sum_{s'=1}^{n'+1} \xi_{r'}\eta_{s'} \left[\alpha^{n'}_{s'} M_1(\hat{\mathbf{x}}_{rs}, \hat{\mathbf{y}}^{r's'}_{rs}) + M_2(\hat{\mathbf{x}}_{rs}, \hat{\mathbf{y}}^{r's'}_{rs})\right] \\ &\times \sum_{|\tilde{j}|\le l} e^{i(j-\tilde{j})\phi_r} F_{sl\tilde{j}j} c^{\tilde{j}}_l P^{|\tilde{j}|}_l(\cos\Theta_{s'}) e^{i\tilde{j}\Phi_{r'}} c^{j'}_{l'} P^{|j'|}_{l'}(\cos\theta_s) e^{-ij'\phi_r}. \end{aligned} \tag{3.34}$$

Thus, the combined acoustic layer $d\times d$ matrix $\mathbf{M}$ with $O(n^4)$ elements, can be set up by successively computing each of the following arrays depending on the four labels (each of which is sum with at most $2n'+2$ elements) can be computed in $O(n^5) = O(d^{2.5})$ operations:

$$E^1_{srs'\tilde{j}} = \sum_{r'=0}^{2n'+1} \xi_{r'} M_1(\hat{\mathbf{x}}_{rs}, \hat{\mathbf{y}}^{r's'}_{rs}) e^{i\tilde{j}\Phi_{r'}}, \qquad E^2_{srs'\tilde{j}} = \sum_{r'=0}^{2n'+1} \xi_{r'} M_2(\hat{\mathbf{x}}_{rs}, \hat{\mathbf{y}}^{r's'}_{rs}) e^{i\tilde{j}\Phi_{r'}},$$

$$D_{srl\tilde{j}} = \sum_{s'=1}^{n'+1} \eta_{s'} \left[\alpha^{n'}_{s'} E^1_{srs'\tilde{j}} + E^2_{srs'\tilde{j}}\right] c^{\tilde{j}}_l P^{|\tilde{j}|}_l(\cos\Theta_{s'}),$$

$$C_{srlj} = \sum_{|\tilde{j}|\le l} D_{srl\tilde{j}} e^{i(j-\tilde{j})\phi_r} F_{sl\tilde{j}j}, \qquad B_{sj'lj} = \sum_{r=0}^{2n+1} C_{srlj} \mu_r e^{-ij'\phi_r},$$

$$\mathbf{M}_{l'j',lj} = \sum_{s=1}^{n+1} B_{sj'lj} \nu_s c^{j'}_{l'} P^{|j'|}_{l'}(\cos\theta_s).$$

The arrays E^1, E^2, are computed, stored, used to compute D and can then be discarded. Then arrays D, C, B and M are computed from each other in a similar way. The result is an algorithm of complexity $O(n^5)$.

The fast Fourier transform (FFT) can be used to speed up the calculation of the above arrays in the longitudinal direction and for calculating F in (3.31). Further, for spherical harmonics of degrees over 100, the fast transform for spherical harmonics (or fast Legendre transform along the latitudinal direction, see [17] and references therein) can be used to reduce the complexity. (For the computational results presented in §4, we used only the FFT, since in our superalgebraically convergent algorithm, spherical harmonics of degree less than 100 are enough to achieve good accuracy even for large acoustic obstacles of size up to 24 times the wavelength.)

In the next two subsections, we describe the second part of our algorithm to compute approximate scattered and far fields using the approximate density W_n of the combined single–double layer acoustic operators.

3.4 Fully discrete approximations on the exterior region

We outline how our numerical solution of the surface integral equation (2.3) can be used to obtain approximate PDE solutions in the exterior by approximating (2.7). The exact solutions on the exterior region, given by (2.10), (2.14) and (2.17) can be written in the general form

$$\begin{aligned} w(\mathbf{x}) &= \int_{\partial D} \left[\tilde{m}(\mathbf{x},\mathbf{y})w(\mathbf{y}) + \tilde{n}(\mathbf{x},\mathbf{y})\tilde{h}(\mathbf{y})\right] ds(\mathbf{y}) \\ &= \int_{\partial B} \left[\tilde{M}_{\mathbf{x}}(\hat{\mathbf{y}})W(\hat{\mathbf{y}}) + \tilde{N}_{\mathbf{x}}(\hat{\mathbf{y}})\tilde{H}(\hat{\mathbf{y}})\right] ds(\hat{\mathbf{y}}), \qquad \mathbf{x} \in \mathbb{R}^3 \setminus \bar{D}, \end{aligned} \tag{3.35}$$

where for each fixed $\mathbf{x} \in \mathbb{R}^3 \setminus \bar{D}$, the smooth functions $\tilde{M}_{\mathbf{x}}$, $\tilde{N}_{\mathbf{x}}$ and $\tilde{H}$ are defined, for $\hat{\mathbf{y}} \in \partial B$, as

$$\tilde{M}_{\mathbf{x}}(\hat{\mathbf{y}}) := \tilde{m}\left(\mathbf{x}, \boldsymbol{q}(\hat{\mathbf{y}})\right) J(\hat{\mathbf{y}}); \quad \tilde{N}_{\mathbf{x}}(\hat{\mathbf{y}}) := \tilde{n}\left(\mathbf{x}, \boldsymbol{q}(\hat{\mathbf{y}})\right) J(\hat{\mathbf{y}}), \quad \tilde{H}(\hat{\mathbf{y}}) = \tilde{h}(\boldsymbol{q}(\hat{\mathbf{y}})), \tag{3.36}$$

and W is the unique solution of (2.30).

Since we can compute a superalgebraic approximation W_n to W, given by (3.16), and since smooth data $\tilde{H}$ on ∂B can be well approximated by $\mathcal{L}_n\tilde{H}$, a natural approximation $w_n(\mathbf{x})$ to $w(\mathbf{x})$, $\mathbf{x} \in \mathbb{R}^3 \setminus \bar{D}$ is given by

$$\begin{aligned} w_n(\mathbf{x}) &= \int_{\partial B} \left[\tilde{M}_{\mathbf{x}}(\hat{\mathbf{y}})W_n(\hat{\mathbf{y}}) + \tilde{N}_{\mathbf{x}}(\hat{\mathbf{y}})\mathcal{L}_n\tilde{H}(\hat{\mathbf{y}})\right] ds(\hat{\mathbf{y}}), \\ &= \sum_{l=0}^{n} \sum_{|j|\le l} \left\{ \omega_{lj} \int_{\partial B} \tilde{M}_{\mathbf{x}}(\hat{\mathbf{y}}) Y_{l,j}(\hat{\mathbf{y}}) ds(\hat{\mathbf{y}}) + \tilde{h}_{lj} \int_{\partial B} \tilde{N}_{\mathbf{x}}(\hat{\mathbf{y}}) Y_{l,j}(\hat{\mathbf{y}}) ds(\hat{\mathbf{y}}) \right\}, \end{aligned} \tag{3.37}$$

where ω_{lj} is the solution of (3.18) and $\tilde{h}_{lj} = (\tilde{H}, Y_{l,j})_m$.

However, since the integrals in (3.37) cannot be evaluated analytically, w_n is not a practically computable approximation. We resolve this problem by instead computing the fully discrete approximation (again denoted by w_n) given by the formula

$$w_n(\mathbf{x}) = \sum_{l=0}^{n} \sum_{|j|\le l} \left\{ \omega_{lj} \int_{\partial B} (\overline{\mathcal{L}}_n\tilde{M}_{\mathbf{x}})(\hat{\mathbf{y}}) Y_{l,j}(\hat{\mathbf{y}}) ds(\hat{\mathbf{y}}) + \tilde{h}_{lj} \int_{\partial B} (\overline{\mathcal{L}}_n\tilde{N}_{\mathbf{x}})(\hat{\mathbf{y}}) Y_{l,j}(\hat{\mathbf{y}}) ds(\hat{\mathbf{y}}) \right\}, \tag{3.38}$$

where $\overline{\mathcal{L}}_n : C(\partial B) \to \mathbb{P}_n$, is the conjugate form of the discrete operator in (2.44), defined as

$$\overline{\mathcal{L}}_n \Psi \;=\; \sum_{l=0}^{n} \sum_{|j|\le l} (\Psi, \overline{Y}_{l,j})_m \overline{Y}_{l,j}, \qquad\qquad \Psi \in C(\partial B). \tag{3.39}$$

Using (3.39), the orthonormality of spherical harmonics and (2.41), we get

$$\begin{aligned} w_n(\mathbf{x}) &= \sum_{l=0}^{n} \sum_{|j|\le l} \left\{ \omega_{lj} \left(\tilde{M}_{\mathbf{x}}, \overline{Y}_{l,j} \right)_m + \tilde{h}_{lj} \left(\tilde{N}_{\mathbf{x}}, \overline{Y}_{l,j} \right)_m \right\} \\ &= \sum_{l=0}^{n} \sum_{|j|\le l} \left\{ \omega_{lj} \tilde{M}_{lj}^m(\mathbf{x}) + \tilde{h}_{lj} \tilde{N}_{lj}^m(\mathbf{x}) \right\}, \qquad \mathbf{x} \in \mathbb{R}^3 \setminus \bar{D}, \end{aligned} \tag{3.40}$$

where for $l = 0, \cdots, n,\ |j| \le l$, the quantities $\tilde{M}_{lj}^m(\mathbf{x}) := \sum_{q=1}^m \zeta_q \tilde{M}_{\mathbf{x}}(\hat{\mathbf{x}}_q) Y_{l,j}(\hat{\mathbf{x}}_q)$ and $\tilde{N}_{lj}^m(\mathbf{x}) := \sum_{q=1}^m \zeta_q \tilde{N}_{\mathbf{x}}(\hat{\mathbf{x}}_q) Y_{l,j}(\hat{\mathbf{x}}_q)$ can be pre-computed, independently of the assembly of (3.18).

3.5 Fully discrete approximations of far field patterns

Our approach to compute approximations, denoted by $w_{n,\infty}$, to the far field pattern w_∞ in (2.8) is analogous to the exterior region computation described in §3.4. The main changes are to replace $\tilde{M}_{\mathbf{x}},\ \tilde{N}_{\mathbf{x}}$ by $M^f_{\hat{\mathbf{x}}},\ N^f_{\hat{\mathbf{x}}},\ \ \hat{\mathbf{x}} \in \partial B$, where

$$M^f_{\hat{\mathbf{x}}}(\hat{\mathbf{y}}) := m^f\left(\hat{\mathbf{x}}, \boldsymbol{q}(\hat{\mathbf{y}})\right) J(\hat{\mathbf{y}}); \qquad N^f_{\hat{\mathbf{x}}}(\hat{\mathbf{y}}) := n^f\left(\hat{\mathbf{x}}, \boldsymbol{q}(\hat{\mathbf{y}})\right) J(\hat{\mathbf{y}}), \quad \hat{\mathbf{y}} \in \partial B. \tag{3.41}$$

Thus our fully discrete approximation to the far field pattern w_∞ of the solution w of (2.7) at any given direction $\hat{\mathbf{x}} \in \partial B$ is defined as

$$w_{n,\infty}(\hat{\mathbf{x}}) := \sum_{l=0}^{n} \sum_{|j|\le l} \left\{ \omega_{lj} M_{lj}^{f,m}(\hat{\mathbf{x}}) + \tilde{h}_{lj} \tilde{N}_{lj}^{f,m}(\hat{\mathbf{x}}) \right\}, \qquad \mathbf{x} \in \mathbb{R}^3 \setminus \bar{D}, \tag{3.42}$$

where for $l = 0, \cdots, n,\ |j| \le l$, the quantities $M_{lj}^{f,m}(\hat{\mathbf{x}}) := \sum_{q=1}^m \zeta_q M^f_{\hat{\mathbf{x}}}(\hat{\mathbf{x}}_q) Y_{l,j}(\hat{\mathbf{x}}_q)$ and $N_{lj}^{f,m}(\hat{\mathbf{x}}) := \sum_{q=1}^m \zeta_q N^f_{\hat{\mathbf{x}}}(\hat{\mathbf{x}}_q) Y_{l,j}(\hat{\mathbf{x}}_q)$.

We prove in the Appendix, under suitable conditions, the superalgebraic convergence of w_n to the solution w of (2.3) on the exterior region, and of the approximate far field pattern $w_{n,\infty}$ to the actual far field pattern w_∞ (see Theorems A.2 and A.3). The results ((A.3), (A.7) and (A.11)) suggest that to compute accurate approximate solutions, it should be enough set up and solve relatively small $d = (n+1)^2$ dimensional systems of the form (3.18). In practice we found that $n \le 20$ is sufficient for frequencies in the resonance region and $n < 100$ for high frequency scattering (with wavelengths about 0.04 times the size of obstacles). In contrast, for high frequency scattering, algorithms [3, 4, 20] require about a quarter to half a million unknowns (but of course these latter algorithms use efficient fast techniques such as the multipole algorithm to create practical codes).

4 Numerical experiments

In this section, we use our algorithm to compute scattered and far fields induced by plane waves impinging on a variety of smooth and non–smooth (sound–soft, sound–hard and absorbing) three dimensional obstacles with Dirichlet, Neumann and Robin boundary conditions. We consider frequencies in the resonance region (with size of the obstacle close to one wavelength) as well as large obstacles with acoustic size up to 24 times the wavelength. We compare the efficiency of our algorithm (denoted by (GG) in the tables below) with other recent algorithms for this problem [3, 4, 6, 20]. In particular, our main comparison is with a recent algorithm of Bruno and Kunyansky (BK) which has been applied in [3, 4] to the exterior Helmholtz equation with Dirichlet boundary condition . The BK algorithm has been demonstrated in [3, 4] to be very competitive in comparison with other recent codes such as [20] and [6] (although the latter algorithms are for electromagnetic scattering).

For numerical experiments, we use various smooth and non–smooth obstacles with diameter siz_obs. These include spherical, ellipsoidal, bean, peanut, ogive, NASA almond and cone–sphere shaped three dimensional domains with corresponding surfaces denoted respectively by $\mathbf{sph}(siz\_obs)$, $\mathbf{ell}(a,b,c)$, $\mathbf{bean}(siz\_obs)$, $\mathbf{pea}(siz\_obs,\alpha)$, $\mathbf{ogive}(siz\_obs)$, $\mathbf{NASA\_alm}(siz\_obs)$ and $\mathbf{cone\_sph}(siz\_obs)$.

For the ellipsoid, the x,y,z axes diameters are respectively a,b,c so that $siz\_obs = \max\{a,b,c\}$. The bean shaped obstacle $\mathbf{bean}(siz\_obs)$ is defined using a radius parameter R (with $siz\_obs = 2R$) by the equation [3]

$$\frac{x^2}{0.64\left(1-0.1\cos\frac{\pi z}{R}\right)} + \frac{\left(0.3R\cos\frac{\pi z}{R}+y\right)^2}{0.64\left(1-0.4\cos\frac{\pi z}{R}\right)} + z^2 = R^2.$$

The peanut shaped obstacle with $siz\_obs = 1$ and angle parameter α is defined implicitly as:

$$x^2 + \frac{y^2}{4} + z^2 = R(z,\alpha),$$

where

$$R(z,\alpha) = c(\alpha)^{-1}\left[p(z)+\sqrt{\alpha+p^2(z)}\right], \qquad p(z) = 2z^2-1, \qquad c(\alpha) = 4\left(1+\sqrt{\alpha+1}\right).$$

The parameter $\alpha > 0$ in $\mathbf{pea}(siz\_obs,\alpha)$ determines the narrowness in the middle of the peanut shape, and as $\alpha \to 0$ the surface becomes more constricted along its equator in the plane $z = 0$.

The ogive, NASA almond and cone–sphere obstacles are defined and used as benchmark radar targets for electromagnetic scattering in [23]. These targets can be described using the spherical coordinate system as below (see Figure 4.1):

$$\mathbf{ogive}(10) = \left\{(q_1^o(\theta),\ q_2^o(\theta,\phi),\ q_3^o(\theta,\phi)) \in \mathbb{R}^3 : 0 \le \theta \le \pi,\ \ 0 \le \phi \le 2\pi\right\},$$

where

$$\begin{aligned} q_1^o(\theta) &= -5 + 10\theta/\pi, \quad q_2^o(\theta,\phi) = f(\theta)\cos(\phi-\pi)/d_o, \quad q_3^o(\theta,\phi) = f(\theta)\sin(\phi-\pi)/d_o, \\ f(\theta) &= \sqrt{1-(q_1^o(\theta)/5)^2\sin^2(22.62^o)} - 1 + d_o, \qquad d_o = 1-\cos(22.62^o). \end{aligned}$$

$$\textbf{NASA\_alm}(9.936) = \left\{(q_1^a(\theta),\ q_2^a(\theta,\phi),\ q_3^a(\theta,\phi)) \in \mathbb{R}^3 : 0 \le \theta \le \pi,\quad 0 \le \phi \le 2\pi\right\},$$

where

$$q_1^a(\theta) = d_a t, \quad t = -\alpha_a + \theta/\pi, \quad d_a = 9.936, \quad \alpha_a = 0.41667,\ \beta_a = 2.08335,\ \gamma_a = 0.96,$$

with $g(t,a) = \sqrt{1-(t/a)^2}$, $\quad \psi = \phi - \pi$, $\quad$ for $-\alpha_a \le t \le 0$,

$$q_2^a(\theta,\phi) = 0.193333\ d_a g(t,\alpha_a)\cos(\psi), \quad q_3^a(\theta,\phi) = 0.064444\ d_a g(t,\alpha_a)\sin(\psi),$$

and for $0 < t \le 0.58333$

$$q_2^a(\theta,\phi) = 4.83345\ d_a\left[g(t,\beta_a) - \gamma_a\right]\cos(\psi), \quad q_3^a(\theta,\phi) = 1.61115\ d_a\left[g(t,\beta_a) - \gamma_a\right]\sin(\psi).$$

$$\textbf{cone\_sph}(27.127) = \left\{(q_1^c(\theta),\ q_2^c(\theta,\phi),\ q_3^c(\theta,\phi)) \in \mathbb{R}^3 : 0 \le \theta \le \pi,\quad 0 \le \phi \le 2\pi\right\},$$

where

$$q_1^c(\theta) = t, \quad t = -\alpha_c + \theta(\beta_c + \alpha_c)/\pi, \quad \alpha_c = 23.821, \quad \beta_c = 3.306, \quad \gamma_c = 2.947,$$

with $h_1(t) = \gamma_c\sqrt{1-((t-0.359)/\gamma_c)^2}$, $\quad h_2(t) = h_1(0)(t+\alpha_c)/\alpha_c$, $\quad \psi = \phi - \pi$,

$$\begin{aligned} q_2^a(\theta,\phi) &= h_2(t)\cos(\psi), \quad q_3^a(\theta,\phi) = h_2(t)\sin(\psi), \qquad \text{for} \quad -\alpha_c \le t \le 0, \\ q_2^a(\theta,\phi) &= h_1(t)\cos(\psi), \quad q_3^a(\theta,\phi) = h_1(t)\sin(\psi), \qquad \text{for} \qquad 0 < t \le \beta_c. \end{aligned}$$

We considered sound–soft, sound–hard and absorbing acoustic scattering problems induced by plane waves with various incident directions and computed the resulting scattered and far fields over a thousand observed directions. Throughout this section, for the plane waves case, the exact far field is denoted by $u_\infty^{\mathbf{pw}}$ and the approximated far field pattern, computed using the solution W_n described in §§ 3.2, 3.5 is denoted by $u_{n,\infty}^{\mathbf{pw}}$.

We know the analytical representation of $u_\infty^{\mathbf{pw}}$ only for the sound–soft sphere case, so for plane wave scattering from other objects we are unable to compute exact errors. Thus, in order to calculate errors and demonstrate the convergence of our algorithm in the case of other scatterers, we compute the far field induced by an off–centre source of radiation inside all our experimental scatterers. We used the Dirichlet, Neumann and Robin boundary conditions induced on the scatterers by the off-centre point source located inside the obstacle at a distance 0.1 from the origin in the direction $\theta = 30^o, \phi = 90^o$. In this case the exact solution is known, it is the field created by the source itself. For the point source radiation case, we denote corresponding exact far field by u_∞ and our computed far field by $u_{n,\infty}$. For the case of non–spherical acoustic scattering, for comparison with [3, 4, 5], we will present maximum norm errors for the far field induced by the point source radiation.

A convergence study of this type gives a good demonstration of the efficiency of an acoustic scattering algorithm based on solving integral equations. However, to get a firm idea of accuracy, it is also practically important to study the convergence of far fields induced by plane waves, for example by fixing some forward and backward incident and observed directions. Such convergence results have been tabulated for

two–dimensional non–spherical scattering in [8, p.72]. Accordingly, following [3, 4, 5] and [8], we also give an extensive convergence study of far fields induced by plane wave incident fields. Here we do not give a comparison with other methods (this case is not reported in [3, 4, 5]). However we remark that (as one may observe from results below for ellipsoidal obstacles), one may get faster convergence in the far field induced by a point source than for that induced by a plane wave with the same frequency. This is naturally due to the less oscillatory behaviour of the boundary data induced by the former. Hence a convergence study of both cases seems to be necessary in order to get a good idea of how an algorithm will perform in practice.

In order to demonstrate superalgebraic convergence in the supremum norm, we computed the errors $\|u_\infty^{\mathbf{pw}} - u_{n,\infty}^{\mathbf{pw}}\|_\infty$ (for spherical obstacles) and $\|u_\infty - u_{n,\infty}\|_\infty$, by taking the maximum of errors obtained over 1300 observed directions. Similar to other algorithms, our computational (and theoretical) convergence results depend on the shape and acoustic size ($k \times siz\_obs$) of a chosen obstacle. As in [3, 4, 5], our results below demonstrate that spherical and ellipsoidal obstacles require fewer degrees of freedom compared to the bean (and peanut) shaped obstacle and that the number of unknowns is dictated by the acoustic size $k \times siz\_obs$ (or equivalently by siz_obj/λ, where $\lambda = 2\pi/k$ is the wavelength).

We used a direct (LU–factorization) solver for the resulting full complex matrix systems. The linear systems which we have to solve, although dense, are sufficiently small so that we could use a direct solver (dimension about 9000 is the largest system solved in this paper). The CPU times given in this work are compared with results obtained using a GMRES solver in [3, 4, 5]. The memory requirement in our computations is essentially dominated by allocating memory for a $d \times d$ full complex matrix. Accordingly, memory allocation in our algorithm is not as efficient as in [3, 4, 5].

In the tabulated results, the L^2 norm relative pointwise RMS error in $|u_\infty^{\mathbf{pw}}(\hat{\mathbf{x}})|^2$, denoted by $\epsilon_{\%}$, the relative L^2 norm, denoted by ϵ_2 and the maximum norm ϵ_∞ are defined as [3]

$$\epsilon_{\%} = 100 \left\{ \frac{1}{4\pi} \int_{\partial B} \left[\left(|u_\infty^{\mathbf{pw}}(\hat{\mathbf{x}})|^2 - \left|u_{n,\infty}^{\mathbf{pw}}(\hat{\mathbf{x}})\right|^2 \right) / |u_\infty^{\mathbf{pw}}(\hat{\mathbf{x}})|^2 \right]^2 ds(\hat{\mathbf{x}}) \right\}^{1/2}, \tag{4.1}$$

$$\epsilon_2 = \left\{ \int_{\partial B} \left|u_\infty^{\mathbf{pw}}(\hat{\mathbf{x}}) - u_{n,\infty}^{\mathbf{pw}}(\hat{\mathbf{x}})\right|^2 ds(\hat{\mathbf{x}}) \right\}^{1/2} \Bigg/ \left\{ \int_{\partial B} \left|u_{n,\infty}^{\mathbf{pw}}(\hat{\mathbf{x}})\right|^2 ds(\hat{\mathbf{x}}) \right\}^{1/2}, \tag{4.2}$$

$$\epsilon_\infty = \|u_\infty^{\mathbf{pw}} - u_{n,\infty}^{\mathbf{pw}}\|_\infty. \tag{4.3}$$

4.1 Sound–soft smooth obstacle scattering problems

For the exterior Helmholtz problem with Dirichlet boundary conditions, we computed results using the indirect formulation (2.10)–(2.12) with $\gamma = siz\_obs/\lambda$. This is a standard choice - see, e.g. [3]. The tables below demonstrate the high–order accuracy of our algorithm. Indeed in several places convincing exponential convergence is observed, even for small values of n. We compare also the performance of our algorithm with other state–of–the–art high–order scattering algorithms [3, 4, 6, 20]. As in [3, 4], we compare our CPU time with only the matrix setup time reported in [6] for the FastScat and FISC algorithms (and we computed $\epsilon_{\%}$ from ϵ_{dB} errors measured in decibels using the relation $\epsilon_{\%} \approx 10\ln(10)\epsilon_{\mathrm{dB}}$, see [3, p. 108]). The CPU time reported for our algorithm is for the

combined setup and solve phases of the algorithm. However, it should be noted that (as acknowledged in [3]), the FastScat and FISC calculations are for electromagnetic scattering.

In Figures 4.4 and 4.5, we visualise the real part and intensity of the total field induced by a plane wave striking a peanut–shaped sound–soft obstacle of diameter 16λ, as depicted in Figures 4.2 and 4.3.

Scattering by sound–soft obstacles of size 1.0λ				
	sph(1.0λ)	**sph**(1.0λ)	**ell**$(1.0\lambda, 0.75\lambda, 0.50\lambda)$	**ell**$(1.0\lambda, 0.25\lambda, 0.25\lambda)$
	$k = 6.283185$	$k = 6.283185$	$k = 0.785398$	$k = 0.785398$
n	$\|u_\infty^{\mathbf{pw}} - u_{n,\infty}^{\mathbf{pw}}\|_\infty$	$\|u_\infty - u_{n,\infty}\|_\infty$	$\|u_\infty - u_{n,\infty}\|_\infty$	$\|u_\infty - u_{n,\infty}\|_\infty$
05	2.93139 E-03	9.7817 E-05	2.94689 E-03	2.88196 E-02
10	2.23937 E-10	4.8117 E-13	4.47165 E-06	1.88838 E-03
15	6.22260 E-14	2.5713 E-14	1.32438 E-08	8.97334 E-05

Scattering by sound–soft obstacles of size 1.0λ			
	bean(1.0λ)	**pea**$(1.0\lambda, 1.0)$	**pea**$(1.0\lambda, 0.25)$
	$k = 1.570796$	$k = 6.283185$	$k = 6.283185$
n	$\|u_\infty - u_{n,\infty}\|_\infty$	$\|u_\infty - u_{n,\infty}\|_\infty$	$\|u_\infty - u_{n,\infty}\|_\infty$
10	5.85399 E-03	8.93979 E-04	3.10283 E-02
15	2.06106 E-04	1.11009 E-05	2.86259 E-03
20	1.84441 E-05	7.73015 E-08	1.98638 E-04

Performance of GG (present), BK [3, 4], FastScat [6] algorithms						
Scattering of a *plane wave* $e^{ik\hat{\mathbf{x}}.\hat{\mathbf{d}}}$ by a sound–soft sphere of diameter 5.4λ						
Algorithm	Unknowns	Computer	CPU time	$\epsilon_\%$	ϵ_2	ϵ_∞
FastScat (Nystrom)	5400	Sparc 10	1953 secs (setup)	2.23%	-	-
FastScat (Galerkin)	5400	Sparc 10	38803 secs (setup)	0.48%	-	-
BK	5430	Pentium II Xeon 400 MHz	1430 secs	0.0025%	-	-
GG	676 ($n = 25$)	SGI Origin 2400, 400 MHz	62 secs	0.0002%	1.0 E-06	3.2 E-06
BK	93726	Pentium II Xeon 400 MHz	> 16 hours*	-	5.6 E-09	1.6 E-08
GG	961 ($n = 30$)	SGI Origin 2400, 400 MHz	178 secs	2.3 E-09%	1.3 E-11	3.3 E-11

** – approximately, based on 16 hours CPU time for solutions with 87318 unknowns (see [3, 4] or results below for scattering of a plane wave by a sphere of diameter 24λ).*

Scattering by sound–soft obstacles of size 8.0λ				
	$\mathbf{sph}(8.0\lambda)$	$\mathbf{sph}(8.0\lambda)$	$\mathbf{ell}(8.0\lambda, 6.0\lambda, 4.0\lambda)$	$\mathbf{ell}(8.0\lambda, 2.0\lambda, 2.0\lambda)$
	$k = 50.265482$	$k = 50.265482$	$k = 6.283185$	$k = 6.283185$
n	$\|u_\infty^{\mathbf{pw}} - u_{n,\infty}^{\mathbf{pw}}\|_\infty$	$\|u_\infty - u_{n,\infty}\|_\infty$	$\|u_\infty - u_{n,\infty}\|_\infty$	$\|u_\infty - u_{n,\infty}\|_\infty$
30	2.30724 E-03	1.1819 E-12	2.00653 E-06	4.49177 E-04
35	7.85715 E-07	9.0183 E-13	3.97078 E-10	9.76850 E-06
40	4.01820 E-11	6.5099 E-13	1.28945 E-12	4.78929 E-07

Scattering by sound–soft obstacles of size 8.0λ			
	$\mathbf{bean}(8.0\lambda)$	$\mathbf{pea}(8.0\lambda, 1.0)$	$\mathbf{pea}(8.0\lambda, 0.25)$
	$k = 12.566370$	$k = 50.265482$	$k = 50.265482$
n	$\|u_\infty - u_{n,\infty}\|_\infty$	$\|u_\infty - u_{n,\infty}\|_\infty$	$\|u_\infty - u_{n,\infty}\|_\infty$
50	9.85025 E-05	4.94508 E-03	8.58038 E-03
55	3.74617 E-06	3.47032 E-04	1.51612 E-03
60	1.01728 E-07	1.58223 E-05	1.03131 E-04

Scattering by sound–soft obstacles of size 16.0λ				
	$\mathbf{sph}(16.0\lambda)$	$\mathbf{sph}(16.0\lambda)$	$\mathbf{ell}(16.0\lambda, 12.0\lambda, 8.0\lambda)$	$\mathbf{ell}(16.0\lambda, 4.0\lambda, 4.0\lambda)$
	$k = 100.530964$	$k = 100.530964$	$k = 12.566370$	$k = 12.566370$
n	$\|u_\infty^{\mathbf{pw}} - u_{n,\infty}^{\mathbf{pw}}\|_\infty$	$\|u_\infty - u_{n,\infty}\|_\infty$	$\|u_\infty - u_{n,\infty}\|_\infty$	$\|u_\infty - u_{n,\infty}\|_\infty$
50	6.16346 E-01	3.0132 E-12	7.09172 E-04	4.78117 E-03
55	1.32466 E-02	3.0376 E-12	2.71990 E-06	6.31451 E-05
60	4.42319 E-05	2.6661 E-12	2.09927 E-09	1.27233 E-06

Scattering by sound–soft obstacles of size 16.0λ			
	$\mathbf{bean}(16.0\lambda)$	$\mathbf{pea}(16.0\lambda, 1.0)$	$\mathbf{pea}(16.0\lambda, 0.25)$
	$k = 25.132741$	$k = 100.530964$	$k = 100.530964$
n	$\|u_\infty - u_{n,\infty}\|_\infty$	$\|u_\infty - u_{n,\infty}\|_\infty$	$\|u_\infty - u_{n,\infty}\|_\infty$
80	2.56078 E-03	2.17945 E-01	2.00576 E-01
85	3.12683 E-04	8.30092 E-02	9.63539 E-02
90	2.30818 E-05	2.04694 E-02	3.52205 E-02

Scattering by sound–soft obstacles of size 24.0λ				
	$\mathbf{sph}(24.0\lambda)$	$\mathbf{sph}(24.0\lambda)$	$\mathbf{ell}(24.0\lambda, 18.0\lambda, 12.0\lambda)$	$\mathbf{ell}(24.0\lambda, 6.0\lambda, 6.0\lambda)$
	$k = 150.796447$	$k = 150.796447$	$k = 18.849556$	$k = 18.849556$
n	$\|u_\infty^{\mathbf{pw}} - u_{n,\infty}^{\mathbf{pw}}\|_\infty$	$\|u_\infty - u_{n,\infty}\|_\infty$	$\|u_\infty - u_{n,\infty}\|_\infty$	$\|u_\infty - u_{n,\infty}\|_\infty$
80	3.41556 E-02	2.7120 E-11	2.27858 E-06	8.98950 E-05
85	2.86857 E-04	2.7828 E-11	4.58837 E-09	5.22077 E-07
90	8.21942 E-07	2.7820 E-11	2.93156 E-11	4.06458 E-09

Scattering of a *plane wave* $e^{ik\hat{\mathbf{x}}.\hat{\mathbf{d}}}$ by non-spherical sound–soft obstacles					
Solution: Far Field $u^{\mathbf{pw}}_{n,\infty}(\hat{\mathbf{d}},\hat{\mathbf{x}})$, $u^{\mathbf{pw}}_{n,\infty}(-\hat{\mathbf{d}},\hat{\mathbf{x}})$, $\hat{\mathbf{d}}=[1,0,0]$, $\hat{\mathbf{x}}=[1,1,1]/\sqrt{3}$					
Obstacle	n	Real $(u^{\mathbf{pw}}_{n,\infty}(\hat{\mathbf{d}},\hat{\mathbf{x}}))$	Imag $(u^{\mathbf{pw}}_{n,\infty}(\hat{\mathbf{d}},\hat{\mathbf{x}}))$	Real $(u^{\mathbf{pw}}_{n,\infty}(-\hat{\mathbf{d}},\hat{\mathbf{x}}))$	Imag $(u^{\mathbf{pw}}_{n,\infty}(-\hat{\mathbf{d}},\hat{\mathbf{x}}))$
bean	50	-1.211638040	-0.425347893	-0.703082440	-0.037623628
(8λ)	55	-1.211638015	-0.425347908	-0.703082439	-0.037623683
$k=12.5664$	60	-1.211638014	-0.425347908	-0.703082438	-0.037623685
bean	80	-0.763292922	-1.023656471	-0.524025819	0.098107599
(16λ)	85	-0.763292757	-1.023655960	-0.524025618	0.098107454
$k=25.1327$	90	-0.763292738	-1.023655946	-0.524025593	0.098107445
pea	50	-0.010761380	0.059509554	-0.145594464	-0.113147447
$(8\lambda, 0.25)$	55	-0.010788151	0.059517472	-0.145612450	-0.113153591
$k=50.2655$	60	-0.010790682	0.059517694	-0.145613620	-0.113154213
pea	80	-0.180243971	-0.083941927	-0.207550479	-0.371539315
$(16\lambda, 0.25)$	85	-0.180277359	-0.082725639	-0.207005811	-0.369927890
$k=100.5310$	90	-0.180039932	-0.082676548	-0.206769636	-0.369908324
ell	50	0.842667688	1.188820559	0.160488626	0.846546412
$(16\lambda, 12\lambda, 8\lambda)$	55	0.841248724	1.187593680	0.160922430	0.846980635
$k=12.5664$	60	0.841255001	1.187587092	0.160924812	0.846977625
ell	80	-1.400743352	0.300790376	-0.769442036	-0.383459664
$(24\lambda, 18\lambda, 12\lambda)$	85	-1.400745575	0.300780793	-0.769440067	-0.383456025
$k=18.8486$	90	-1.400745555	0.300780760	-0.769440053	-0.383456047

Performance of GG (present), BK [3, 4], FISC [20] algorithms				
Scattering of a *plane wave* $e^{ik\hat{\mathbf{x}}.\hat{\mathbf{d}}}$ by a sound–soft sphere of diameter 24λ				
Algorithm	Unknowns	Computer	CPU time	$\epsilon_{\%}$ (RMS error)
FISC	602112	SGI Power Challenge R8000	12 hours	6.9%
BK	26214	Pentium II Xeon 400 MHz	6.5 hours	0.18%
BK	87318	Pentium II Xeon 400 MHz	16 hours	0.0014%
GG	6889 $(n=82)$	SGI Origin 2400, 400 MHz	5.8 hours	0.19%
GG	7744 $(n=87)$	SGI Origin 2400, 400 MHz	9.3 hours	0.0011%

Performance of GG (present) and BK [5] algorithms					
Scattering by sound–soft non–spherical obstacles					
Obstacle	Algorithm	Unknowns	Computer	CPU time	$\|u_\infty - u_{n,\infty}\|_\infty$
ell $(16\lambda, 12\lambda, 8\lambda)$	BK	265020	AMD 1600+ 1.4 GHz	494 mins	1.3 E-05
	GG	3136 ($n = 55$)	SGI Origin 2400, 400 MHz	47 mins	2.7 E-06
ell $(16\lambda, 4\lambda, 4\lambda)$	BK	199536	AMD 1600+ 1.4 GHz	675 mins	1.4 E-04
	GG	3136 ($n = 55$)	SGI Origin 2400, 400 MHz	47 mins	6.3 E-05
bean (16λ)	BK	238646	AMD 1600+ 1.4 GHz	1003 mins	1.7 E-05
	GG	8649 ($n = 92$)	SGI Origin 2400, 400 MHz	777 mins	7.9 E-06
ell $(24\lambda, 18\lambda, 12\lambda)$	BK	265020	AMD 1600+ 1.4 GHz	858 mins	9.3 E-06
	GG	6561 ($n = 80$)	SGI Origin 2400, 400 MHz	336 mins	2.3 E-06
ell $(24\lambda, 6\lambda, 6\lambda)$	BK	199536	AMD 1600+ 1.4 GHz	720 mins	2.6 E-04
	GG	6561 ($n = 80$)	SGI Origin 2400, 400 MHz	335 mins	9.0 E-05

4.2 Sound–hard smooth obstacle scattering problems

The following selected results demonstrate the power of our algorithm for computations in the resonance and high frequency regions for three dimensional exterior Neumann problems for both the point source radiation and plane wave acoustic scattering.

Scattering by sound–hard obstacles of size 1.1λ - Neumann			
	bean(1.1λ)	**pea**$(1.1\lambda, 1.0)$	**pea**$(1.1\lambda, 0.25)$
	$k = 1.727876$	$k = 6.911504$	$k = 6.911504$
n	$\|u_\infty - u_{n,\infty}\|_\infty$	$\|u_\infty - u_{n,\infty}\|_\infty$	$\|u_\infty - u_{n,\infty}\|_\infty$
10	7.11578 E-02	1.57695 E-03	2.28875 E-02
15	4.66991 E-03	1.16830 E-05	1.48284 E-03
20	5.56065 E-04	7.07394 E-08	1.22790 E-04

Scattering by sound–hard obstacles of size 8.1λ - Neumann			
	bean(8.1λ)	**pea**$(8.1\lambda, 1.0)$	**pea**$(8.1\lambda, 0.25)$
	$k = 12.723450$	$k = 50.893801$	$k = 50.893801$
n	$\|u_\infty - u_{n,\infty}\|_\infty$	$\|u_\infty - u_{n,\infty}\|_\infty$	$\|u_\infty - u_{n,\infty}\|_\infty$
50	2.95234 E-04	8.25592 E-06	1.10301 E-03
55	1.21654 E-05	2.17825 E-07	7.55252 E-05
60	3.59514 E-07	4.05182 E-09	7.38611 E-06

Scattering by sound–hard obstacles of size 16.0λ - Neumann			
	bean(16.0λ)	**pea**$(16.0\lambda, 1.0)$	**pea**$(16.0\lambda, 0.25)$
	$k = 25.132741$	$k = 100.530964$	$k = 100.530964$
n	$\|u_\infty - u_{n,\infty}\|_\infty$	$\|u_\infty - u_{n,\infty}\|_\infty$	$\|u_\infty - u_{n,\infty}\|_\infty$
80	4.20005 E-03	1.44818 E-04	3.40975 E-02
85	3.45799 E-04	8.49506 E-06	1.10705 E-02
90	2.70156 E-05	4.22015 E-07	2.43972 E-03

Scattering of a plane wave $e^{ik\hat{\mathbf{x}}.\hat{\mathbf{d}}}$ by sound–hard obstacles - Neumann					
Solution: Far Field $u^{\mathbf{pw}}_{n,\infty}(\hat{\mathbf{d}}, \hat{\mathbf{x}})$, $u^{\mathbf{pw}}_{n,\infty}(-\hat{\mathbf{d}}, \hat{\mathbf{x}})$, $\hat{\mathbf{d}} = [1,0,0]$, $\hat{\mathbf{x}} = -[1,1,1]/\sqrt{3}$					
Obstacle	n	Real $(u^{\mathbf{pw}}_{n,\infty}(\hat{\mathbf{d}}, \hat{\mathbf{x}}))$	Imag $(u^{\mathbf{pw}}_{n,\infty}(\hat{\mathbf{d}}, \hat{\mathbf{x}}))$	Real $(u^{\mathbf{pw}}_{n,\infty}(-\hat{\mathbf{d}}, \hat{\mathbf{x}}))$	Imag $(u^{\mathbf{pw}}_{n,\infty}(-\hat{\mathbf{d}}, \hat{\mathbf{x}}))$
bean	50	0.415261424	-0.505277949	0.438549342	-1.338746349
(8.1λ)	55	0.415257586	-0.505270217	0.438545727	-1.338751789
$k = 12.7235$	60	0.415257617	-0.505270015	0.438545604	-1.338751798
bean	80	0.559103508	-0.245076660	-0.291237321	-1.378483777
(16.0λ)	85	0.559127902	-0.245065203	-0.291245398	-1.378511528
$k = 25.1327$	90	0.559128870	-0.245064721	-0.291246171	-1.378512892
pea	50	0.026594481	0.128380355	0.006540556	0.001711920
$(8.1\lambda, 0.25)$	55	0.026665734	0.128349275	0.006637935	0.001707533
$k = 50.8938$	60	0.026667821	0.128346121	0.006642237	0.001704709
pea	80	0.041727559	0.349839234	0.089615803	-0.028435947
$(16.0\lambda, 0.25)$	85	0.043566240	0.351311085	0.091114809	-0.026822423
$k = 100.5310$	90	0.043162994	0.350877127	0.090605571	-0.027221696

4.3 Absorbing smooth obstacle scattering problems

We computed approximate solutions of the impedance boundary condition scattering problem with Robin constant $\mu = 1$. As in the Dirichlet and Neumann problem experiments, we obtained good accuracy for all the geometries and the wave numbers considered in this paper. Here is a selection of results.

Scattering by absorbing obstacles of size 1.1λ - Robin $\mu = 1$

	bean(1.1λ)	**pea**$(1.1\lambda, 1.0)$	**pea**$(1.1\lambda, 0.25)$
	$k = 1.727876$	$k = 6.911504$	$k = 6.911504$
n	$\|u_\infty - u_{n,\infty}\|_\infty$	$\|u_\infty - u_{n,\infty}\|_\infty$	$\|u_\infty - u_{n,\infty}\|_\infty$
10	2.84122 E-02	1.54524 E-03	2.38354 E-02
15	1.91105 E-03	1.11917 E-05	1.55407 E-03
20	2.18761 E-04	6.89745 E-08	1.25606 E-04

Scattering by absorbing obstacles of size 8.1λ - Robin $\mu = 1$

	bean(8.1λ)	**pea**$(8.1\lambda, 1.0)$	**pea**$(8.1\lambda, 0.25)$
	$k = 12.723450$	$k = 50.893801$	$k = 50.893801$
n	$\|u_\infty - u_{n,\infty}\|_\infty$	$\|u_\infty - u_{n,\infty}\|_\infty$	$\|u_\infty - u_{n,\infty}\|_\infty$
50	2.64753 E-04	8.25994 E-06	1.07671 E-03
55	1.09092 E-05	2.18623 E-07	7.54619 E-05
60	3.22415 E-07	4.04770 E-09	7.24602 E-06

Scattering by absorbing obstacles of size 16.0λ - Robin $\mu = 1$

	bean(16.0λ)	**pea**$(16.0\lambda, 1.0)$	**pea**$(16.0\lambda, 0.25)$
	$k = 25.132741$	$k = 100.53096$	$k = 100.53096$
n	$\|u_\infty - u_{n,\infty}\|_\infty$	$\|u_\infty - u_{n,\infty}\|_\infty$	$\|u_\infty - u_{n,\infty}\|_\infty$
80	3.86799 E-03	1.40528 E-04	3.36103 E-02
85	3.26862 E-04	8.47871 E-06	1.08972 E-02
90	2.42218 E-05	4.21669 E-07	2.39322 E-03

Scattering of a *plane wave* $e^{ik\hat{\mathbf{x}}.\hat{\mathbf{d}}}$ by absorbing obstacles - Robin $\mu = 1$

Solution: Far Field $u^{\mathbf{pw}}_{n,\infty}(\hat{\mathbf{d}}, \hat{\mathbf{x}})$, $u^{\mathbf{pw}}_{n,\infty}(-\hat{\mathbf{d}}, \hat{\mathbf{x}})$, $\hat{\mathbf{d}} = [1, 0, 0]$, $\hat{\mathbf{x}} = [1, 1, 1]/\sqrt{3}$

Obstacle	n	Real $(u^{\mathbf{pw}}_{n,\infty}(\hat{\mathbf{d}}, \hat{\mathbf{x}}))$	Imag $(u^{\mathbf{pw}}_{n,\infty}(\hat{\mathbf{d}}, \hat{\mathbf{x}}))$	Real $(u^{\mathbf{pw}}_{n,\infty}(-\hat{\mathbf{d}}, \hat{\mathbf{x}}))$	Imag $(u^{\mathbf{pw}}_{n,\infty}(-\hat{\mathbf{d}}, \hat{\mathbf{x}}))$
bean	50	1.157322289	-0.215292184	0.311971960	-0.362405347
(8.1λ)	55	1.157313018	-0.215289339	0.311975072	-0.362401148
$k = 12.7235$	60	1.157312917	-0.215289154	0.311975191	-0.362401065
bean	80	0.928403718	0.886621134	0.284685356	-0.166745117
(16.0λ)	85	0.928415863	0.886629309	0.284678019	-0.166760975
k =25.1327	90	0.928416373	0.886629785	0.284677674	-0.166761669
pea	50	0.005081427	0.000776985	0.022830804	0.124490732
$(8.1\lambda, 1.0)$	55	0.005172910	0.000780003	0.022899996	0.124466732
$k = 50.8938$	60	0.005176831	0.000778074	0.022901998	0.124464350
pea	80	0.085105780	-0.025378131	0.038948001	0.345352189
$(16.0\lambda, 0.25)$	85	0.086474020	-0.023845559	0.040625060	0.346789662
$k = 100.5310$	90	0.085995837	-0.024256504	0.040245496	0.346359508

4.4 Non–smooth obstacle scattering

In this section, we demonstrate fast convergence of our algorithm for obstacles with conical singularities for frequencies in the resonance region and compare our results with those given in [4]. In this paper, for the non–smooth obstacles, we restrict to low frequency scattering and we present our results for the sound–soft case. We find that, despite the non-smoothness of the domain, reasonable accuracy is still obtained, especially for the NASA almond and ogive examples.

Scattering by sound–soft obstacles of size 1.0λ			
	NASA_alm(1.0λ)	**ogive**(1.0λ)	**cone_sph**(1.0λ)
	$k = 0.6283185$	$k = 0.6323657$	$k = 0.2316211$
n	$\|u_\infty - u_{n,\infty}\|_\infty$	$\|u_\infty - u_{n,\infty}\|_\infty$	$\|u_\infty - u_{n,\infty}\|_\infty$
05	6.73728 E-02	2.30540 E-02	2.18547 E-01
15	3.15581 E-03	1.40747 E-04	6.35614 E-02
25	2.68313 E-04	8.31994 E-05	3.27117 E-02

Performance of GG (present), BK [4] algorithms				
Scattering by one–wavelength long sound–soft ogive				
Algorithm	Unknowns	Computer	CPU time	$\|u_\infty - u_{n,\infty}\|_\infty$
BK	1568	Pentium II Xeon 400 MHz	1380 secs	2.5 E-03
GG	256 ($n = 15$)	SGI Origin 2400, 400 MHz	16 secs	1.4 E-04
BK	6336	Pentium II Xeon 400 MHz	13005 secs	3.8 E-05
GG	676 ($n = 25$)	SGI Origin 2400, 400 MHz	173 secs	8.3 E-05

Acknowledgements

Financial support of the Australian Research Council and the University of New South Wales is gratefully acknowledged. The authors thank Professor Ian Sloan for helpful advice and Professors Oscar Bruno and Leonid Kunyansky for providing new numerical results [5] for comparison with our algorithm. The first author is also grateful to Mr. Dave Dowsett for coding assistance; and to Mr. Jakob Bjerkemo and Mr. Paul Leopardi for help with visualisation. Computations were carried out using CPU time allotted to the first author by the Australian Centre for Advanced Computing and Communications (ac3) and M. Ganesh thanks ac3 for supporting the project.

References

[1] K.E. Atkinson, *The Numerical Solution Integral Equations of the Second Kind*, Cambridge University Press, Cambridge, 1997.

[2] D.M. Brink and G.R. Satchler, *Angular Momentum*, Second Edition, Clarendon Press, Oxford, 1968.

[3] O.P. Bruno and L.A. Kunyansky, A fast, high-order algorithm for the solution of surface scattering problems: basic implementation, tests and applications, *J. Comp. Phys.*, 169(2001), 80–110.

[4] O.P. Bruno and L.A. Kunyansky, Surface scattering in three dimensions: an accelerated high-order solver, *Proc. Roy. Soc. London A*, 457 (2001), 2721–2934.

[5] O.P. Bruno and L.A. Kunyansky, Private communication.

[6] L. Canino, J.Ottusch, M. Stalzer, J. Visher and S. Wandzura, Numerical solution of the Helmholtz equation in 2D and 3D using a high–order Nystrom discretization, *J. Comp. Phys.*, 146 (1998), 627–663.

[7] D. Colton and R. Kress, *Integral equation methods in Inverse Scattering Theory.* Wiley, 1983.

[8] D. Colton and R. Kress, *Inverse Acoustic and Electromagnetic Scattering Theory.* Spinger-Verlag, 1998.

[9] D. Colton, J. Coyle and P. Monk, Recent developments in inverse acoustic scattering theory, *SIAM Review* 42 (2000), 369–414.

[10] M. Ganesh, I.G. Graham and J. Sivaloganathan, A pseudospectral 3D boundary integral method applied to a nonlinear model problem from finite elasticity, *SIAM J. Numer. Anal.* 31 (1994), 1378-1414.

[11] M.Ganesh, I.G. Graham and J. Sivaloganathan, A new spectral boundary integral collocation method for three-dimensional potential problems, *SIAM J. Numer. Anal.* 35 (1998), 778-805.

[12] K. Gerdes, A review of infinite element methods for exterior Helmholtz problems, J. Comp. Acoustics 8 (2000) 43–62.

[13] I.G. Graham and I.H. Sloan, Fully discrete spectral boundary integral methods on smooth closed surfaces in $\mathbb{R}^3$, *Numer. Math.*, 92 (2002), 289-323.

[14] A. Kirsch and P. Monk, An analysis of the coupling of finite element and Nystrom methods in acoustic scattering, *IMA J. Numer. Anal.*, 14 (1994), 523-544.

[15] T.C. Lin, The numerical solution of Helmholtz's equation for the exterior problem in three dimensions, *SIAM J. Numer. Anal.* 22 (1985), 670–686.

[16] T.C. Lin and Y. Warnapala–Yehiya, The numerical solution of exterior Dirichlet problem for Helmholtz's equation via modified Green's functions approach, *Comp. Math. Appls.* 44 (2002), 1229–1248.

[17] M.J. Mohlenkamp A fast transform for spherical harmonics, *J. Fourier Anal. Appls.* 5(1999), 159–184.

[18] J.C. Nedelec, *Acoustic and Electromagnetic Equations*. Spinger-Verlag, 2000.

[19] I.H. Sloan and R.S. Womersley, Constructive approximation on the sphere *J. Approx. Theory*, 103 (2000), 91-118.

[20] J.M. Song, C.C. Lu, W.C. Chew and S.W. Lee, Fast Illinois Solver Code (FISC), *IEEE Antennas Propag. Mag.*, 40 (1998), 27–34.

[21] G. Szegö, *Orthogonal Polynomials*, American Mathematical Society Colloquium Publications, Volume XXIII, New York, 1959.

[22] L. Wienert, *Die numerische Approximation von Randintegraloperatoren für die Helmholtzgleichung im* $\mathbb{R}^3$. PhD thesis, University of Göttingen, 1990.

[23] A.C. Woo, H.T.G. Wang, M.J. Schuh and M.L. Sanders, Benchmark radar targets for the validation of computational electromagnetics programs, *IEEE Antennas Propag. Mag.* 35(1993), 84–89.

Appendix

In this section we prove superalgebraic convergence properties of our fully discrete approximations on the surface and on the exterior region, using results in [13] and functional analytic arguments.

Through this section, the space $C(\partial B)$ of continuous functions on ∂B is equipped with the uniform norm $\|\cdot\|_{\infty,\partial B}$ and we also use the same notation for the corresponding operator norm. For $r > 0$, $C^r(\partial B)$ denotes the space of all r times continuously differentiable functions on ∂B. We use similar notation for ∂D and assume that the parametrisation map $\boldsymbol{q} : \partial B \to \partial D$ is smooth.

The hyperinterpolation operator defined in (2.44) has the following crucial boundedness and approximation properties [19]:

$$\|\mathcal{L}_n\|_{\infty,\partial B} \le cn^{1/2}, \qquad \|\mathcal{L}_n\Psi - \Psi\|_{\infty,\partial B} \le c_r \frac{1}{n^{r-1/2}} \|\Psi\|_{r,\partial B}, \quad \Psi \in C^r(\partial B), \tag{A.1}$$

where (throughout this section) $c, c_r, c_{\ell,r}$ are generic constants independent of the approximation parameter n. (The conjugate operator $\overline{\mathcal{L}}_n$ in (3.39) also satisfies the bounds in (A.1).) The discrete layer operator $\mathcal{N}_{n'}$ defined in (3.14) is a powerful approximation to $\mathcal{N}$ in the following sense [13, Theorem 5.2]:

$$\|(\mathcal{N}_{n'} - \mathcal{N})\mathcal{L}_n\Psi\|_{\infty,\partial B} \le c_\ell \frac{1}{n^\ell} \|\Psi\|_{\infty,\partial B}, \quad \Psi \in C(\partial B), \text{ and for any } \ell \in \mathbb{N}. \tag{A.2}$$

A similar estimate holds for $\|(\mathcal{M}_{n'} - \mathcal{M})\mathcal{L}_n\Psi\|_{\infty,\partial B}$.

We first prove that our algorithm for solving (2.3) converges superalgebraically.

Theorem A.1 *Let w be the unique solution of (2.3) with a given data h. Let w_n be as in (3.20), where $W_n \in \mathbb{P}_n$ is the unique solution of (3.15). If $h \in C^{r+2}(\partial D)$ for some $r > 0$, then for n sufficiently large n, there exists $c_r > 0$ such that*

$$\|w - w_n\|_{\infty,\partial D} \le c_r \, \frac{1}{n^r} \left\{ \|w\|_{r+1,\partial D} + \|h\|_{r+2,\partial D} \right\}. \tag{A.3}$$

Proof. Following the proof of Theorem 5.1 in [13], we have for sufficiently large n, $(I + \mathcal{L}_n \mathcal{M}_{n'})^{-1}$ exists and $\|(I + \mathcal{L}_n \mathcal{M}_{n'})^{-1}\|_{\infty,\partial B} \le cn^{1/2}$. Hence, for sufficiently large n, (3.15) has a unique solution $W_n \in \mathbb{P}_n$.

Let $U_n \in \mathbb{P}_n$ be the unique solution of

$$U_n + \mathcal{L}_n \mathcal{M}_{n'} U_n = \mathcal{L}_n \left[\alpha I + \mathcal{N} \right] H \ , \tag{A.4}$$

a semi-discrete approximation of (2.30). For such an approximation, a direct application of results in [13] yields the superalgebraic convergence property

$$\|W - U_n\|_{\infty,\partial B} \le c_r \frac{1}{n^r} \|W\|_{r+1,\partial B}, \tag{A.5}$$

Now, using (3.15), (A.4), (A.1), (A.5), and (A.2), we get

$$\begin{aligned}
&\|W - W_n\|_{\infty,\partial B} \\
&\le \|W - U_n\|_{\infty,\partial B} + \|U_n - W_n\|_{\infty,\partial B} \\
&\le \|W - U_n\|_{\infty,\partial B} + \|(I + \mathcal{L}_n \mathcal{M}_{n'})^{-1} \left(\mathcal{L}_n \mathcal{N}_{n'} \mathcal{L}_n H - \mathcal{L}_n \mathcal{N} H \right) \|_{\infty,\partial B} \\
&\le \|W - U_n\|_{\infty,\partial B} + c \ n \| \mathcal{N}_{n'} \mathcal{L}_n H - \mathcal{N} H \|_{\infty,\partial B} \\
&\le \|W - U_n\|_{\infty,\partial B} + c \ n \| \left(\mathcal{N}_{n'} - \mathcal{N} \right) \mathcal{L}_n H \|_{\infty,\partial B} + c \ n \| \mathcal{N} \left(\mathcal{L}_n H - H \right) \|_{\infty,\partial B} \\
&\le c_r \ \frac{1}{n^r} \|W\|_{r+1,\partial B} + c_r \ n \frac{1}{n^{r+1}} \|H\|_{\infty,\partial B} + c_r \ n^{3/2} \frac{1}{n^{r+2}} \|H\|_{r+2,\partial B} \\
&\le c_r \ \frac{1}{n^r} \left\{ \|W\|_{r+1,\partial B} + \|H\|_{r+2,\partial B} \right\}
\end{aligned} \tag{A.6}$$

Finally, from (2.29), (3.20) and (A.6), we get

$$\|w - w_n\|_{\infty,\partial D} \le c \ \|W - W_n\|_{\infty,\partial B} \le c_r \ \frac{1}{n^r} \left\{ \|w\|_{r+1,\partial D} + \|h\|_{r+2,\partial D} \right\}. \qquad \square$$

Next we prove the convergence of approximate solutions in the exterior domain.

Theorem A.2 *Let $w(\mathbf{x}), w_n(\mathbf{x})$, for $\mathbf{x} \in \mathbb{R}^3 \setminus \bar{D}$, be respectively defined by (2.7) and (3.40), for a given data $h \in C^{r+2}(\partial D)$ with $r > 0$. Then, for $\mathbf{x} \in \mathbb{R}^3 \setminus \bar{D}$, and for any $\ell \in \mathbb{N}$, there exist constants $c_r, c_{\ell,r} > 0$, independent of n, such that*

$$\begin{aligned}
|w(\mathbf{x}) - w_n(\mathbf{x})| \ \le \ & c_r \frac{1}{n^r} \left\{ \left| \tilde{M}_{\mathbf{x}} \right|_1 \left(\|W\|_{r+1,\partial B} + \|H\|_{r+2,\partial B} \right) + \left| \tilde{N}_{\mathbf{x}} \right|_1 \|\tilde{H}\|_{r+1,\partial B} \right\} \\
& + c_{\ell,r} \frac{1}{n^{\ell+r}} \left\{ \|\tilde{M}_{\mathbf{x}}\|_{r+\ell,\partial B} \|W\|_{\infty,\partial B} + \|\tilde{N}_{\mathbf{x}}\|_{r+\ell,\partial B} \|\tilde{H}\|_{\infty,\partial B} \right\},
\end{aligned} \tag{A.7}$$

where $|\bullet|_1 := \int_{\partial B} |\bullet(\hat{\mathbf{y}})| \, ds(\hat{\mathbf{y}})$, W is the unique solution of (2.30), $\tilde{M}$, $\tilde{N}$, $\tilde{H}$ are given by (3.36), and $\tilde{H} = 0$ (or H) for the Dirichlet (or the Neumann/Robin) problem.

Proof. We use representations (3.35), (3.37) and (3.38) to prove the result. Let $\mathbf{x} \in \mathbb{R}^3 \setminus \bar{D}$, be fixed. We have, $|w(\mathbf{x}) - w_n(\mathbf{x})| \leq I_1 + I_2$, where

$$\begin{aligned} I_1 &= \int_{\partial B} \left| \tilde{M}_{\mathbf{x}}(\hat{\mathbf{y}}) W(\hat{\mathbf{y}}) - \left(\overline{\mathcal{L}}_n \tilde{M}_{\mathbf{x}} \right)(\hat{\mathbf{y}}) W_n(\hat{\mathbf{y}}) \right| ds(\hat{\mathbf{y}}) \\ &\leq \int_{\partial B} \left| \tilde{M}_{\mathbf{x}}(\hat{\mathbf{y}}) \left(W - W_n \right)(\hat{\mathbf{y}}) \right| ds(\hat{\mathbf{y}}) + \int_{\partial B} \left| \left(\tilde{M}_{\mathbf{x}} - \overline{\mathcal{L}}_n \tilde{M}_{\mathbf{x}} \right)(\hat{\mathbf{y}}) W_n(\hat{\mathbf{y}}) \right| ds(\hat{\mathbf{y}}) \\ &\leq \left| \tilde{M}_{\mathbf{x}} \right|_1 \|W - W_n\|_{\infty,\partial B} + |W_n|_1 \, \|\tilde{M}_{\mathbf{x}} - \overline{\mathcal{L}}_n \tilde{M}_{\mathbf{x}}\|_{\infty,\partial B} \end{aligned} \tag{A.8}$$

and

$$\begin{aligned} I_2 &= \int_{\partial B} \left| \tilde{N}_{\mathbf{x}}(\hat{\mathbf{y}}) \tilde{H}(\hat{\mathbf{y}}) - \left(\mathcal{L}_n \tilde{N}_{\mathbf{x}} \right)(\hat{\mathbf{y}}) \left(\overline{\mathcal{L}}_n \tilde{H} \right)(\hat{\mathbf{y}}) \right| ds(\hat{\mathbf{y}}) \\ &\leq \int_{\partial B} \left| \tilde{N}_{\mathbf{x}}(\hat{\mathbf{y}}) \left(\tilde{H} - \overline{\mathcal{L}}_n \tilde{H} \right)(\hat{\mathbf{y}}) \right| ds(\hat{\mathbf{y}}) + \int_{\partial B} \left| \left(\tilde{N}_{\mathbf{x}} - \overline{\mathcal{L}_n} \tilde{N}_{\mathbf{x}} \right)(\hat{\mathbf{y}}) \overline{\mathcal{L}}_n \tilde{H}(\hat{\mathbf{y}}) \right| ds(\hat{\mathbf{y}}). \\ &\leq \left| \tilde{N}_{\mathbf{x}} \right|_1 \|\tilde{H} - \overline{\mathcal{L}}_n \tilde{H}\|_{\infty,\partial B} + \left| \mathcal{L}_n \tilde{H} \right|_1 \|\tilde{N}_{\mathbf{x}} - \overline{\mathcal{L}}_n \tilde{N}_{\mathbf{x}}\|_{\infty,\partial B}. \end{aligned} \tag{A.9}$$

Using the detailed analysis in [13, 19], it can be shown that $|W_n|_1$ and $\left| \mathcal{L}_n \tilde{H} \right|_1$ are uniformly bounded. Since $\tilde{M}_{\mathbf{x}}, \tilde{N}_{\mathbf{x}}$ are infinitely continuously differentiable on ∂B, applying the estimates (A.1) and (A.6) in (A.8) and (A.9), we get the result (A.7). □

Finally, we obtain the convergence of the approximate far field pattern $w_{n,\infty}$, given by (3.42). Since our approach for computing $w_{n,\infty}$ is analogous to computations on the exterior region (see §3.5), it is easy to see that for a fixed direction $\hat{\mathbf{x}} \in \partial B$, following Theorem A.2, $|w_\infty(\hat{\mathbf{x}}) - w_{n,\infty}(\hat{\mathbf{x}})|$ is bounded by the estimate in (A.7), with $\tilde{M}_{\mathbf{x}}$, $\tilde{N}_{\mathbf{x}}$ replaced respectively by $M^f_{\hat{\mathbf{x}}}$, $N^f_{\hat{\mathbf{x}}}$, defined in (3.41).

Since $m^f(\hat{\mathbf{x}}, \mathbf{y})$, $n^f(\hat{\mathbf{x}}, \mathbf{y})$ are linear combinations of $e^{-ik\hat{\mathbf{x}}.\mathbf{y}}$ and $\partial e^{-ik\hat{\mathbf{x}}.\mathbf{y}}/\partial n(\mathbf{y})$, for $y \in \partial D$, we have for any $\ell \in \mathbb{N}$, and for any $\hat{\mathbf{x}} \in \partial B$,

$$|M_{\hat{\mathbf{x}}}|_1 \leq c\, k, \quad \|M_{\hat{\mathbf{x}}}\|_{\ell,\partial B} \leq c_\ell \, k^{\ell+1}, \qquad \left| N^f_{\hat{\mathbf{x}}} \right|_1 \leq c\, k, \quad \|N^f_{\hat{\mathbf{x}}}\|_{\ell,\partial B} \leq c_\ell \, k^{\ell+1}. \tag{A.10}$$

Consequently, using arguments in Theorem A.2, we get the following result.

Theorem A.3 *Let w_∞ be as in (2.8), for given a data function $h \in C^{r+2}(\partial D)$ with $r > 0$. Let $w_{n,\infty}$ be given by (3.42). Then, for any $\ell \in \mathbb{N}$, there exist constants $c_r, c_{\ell,r} > 0$, independent of n, such that*

$$\begin{aligned} \|w_\infty - w_{n,\infty}\|_{\infty,\partial B} &\leq c_r \frac{1}{n^r} \left\{ \|W\|_{r+1,\partial B} + \|H\|_{r+2,\partial B} + \|\tilde{H}\|_{r+1,\partial B} \right\} \\ &\quad + c_{\ell,r} \left(\frac{1}{n} \right)^{\ell+r} \left\{ \|W\|_{\infty,\partial B} + \|\tilde{H}\|_{\infty,\partial B} \right\}, \end{aligned} \tag{A.11}$$

where W is the unique solution of (2.30), and $\tilde{H} = 0$ (or H) for the Dirichlet (or the Neumann/Robin) problem.

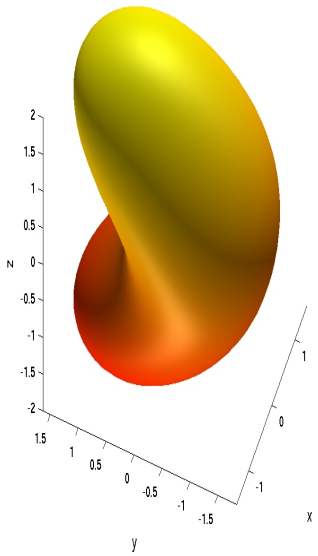

bean(4)

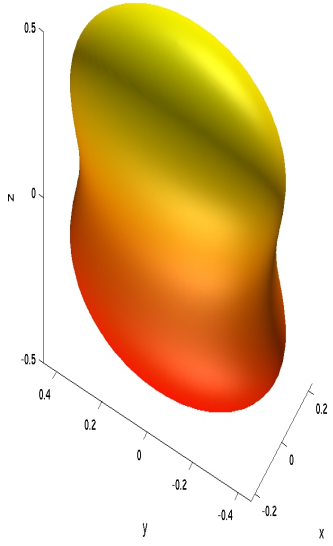

pea(1,1.0)

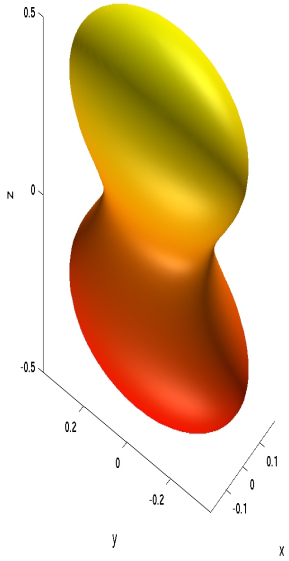

pea(1,0.25)

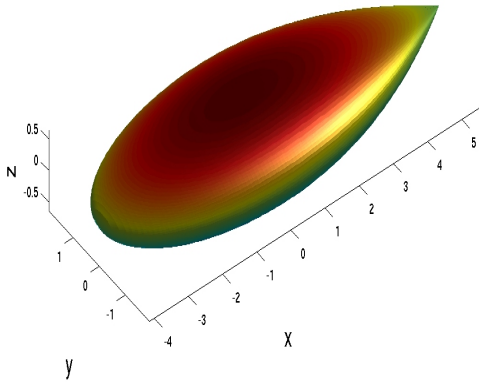

NASA_alm(9.936)

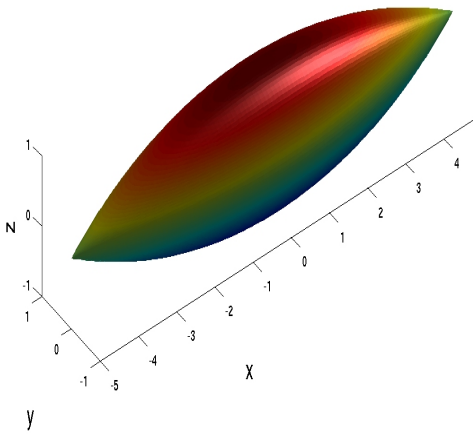

ogive(10)

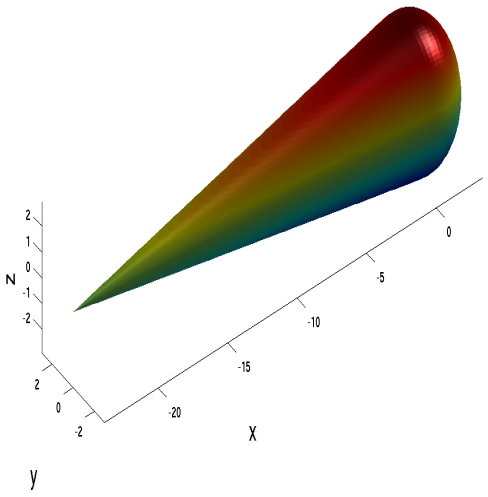

cone_sph(27.127)

Figure 4.1: some of the obstacles used in our computation

Visualisation of scattering of a plane wave $u^I(\mathbf{x}) = e^{ik\mathbf{x}.\hat{\mathbf{d}}}$ (with $k = 100.531$) propagating in the x-direction (with $\hat{\mathbf{d}} = [1\ 0\ 0]$) by a peanut shaped sound–soft obstacle of size sixteen times the wavelength $\lambda = 2\pi/k$, on a yz-plane.

The scattered field is denoted by u^S and the total field is $u = u^I + u^S$

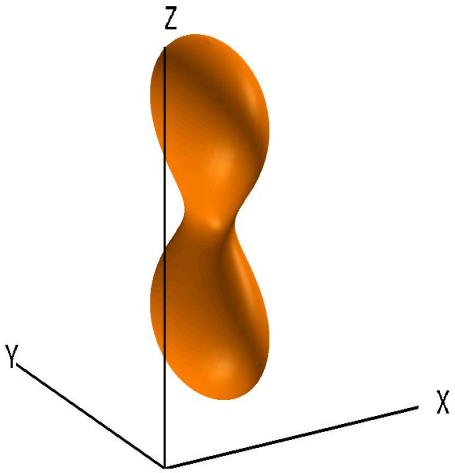

Figure 4.2: obstacle pea$(16\lambda, 0.25)$

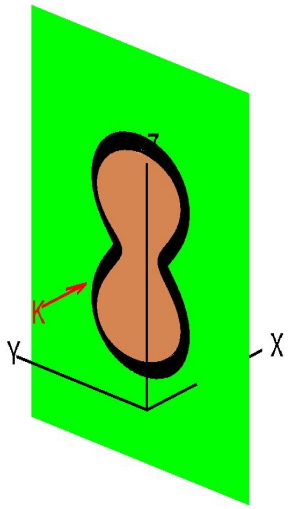

Figure 4.3: $yz-$plane through pea$(16\lambda, 0.25)$

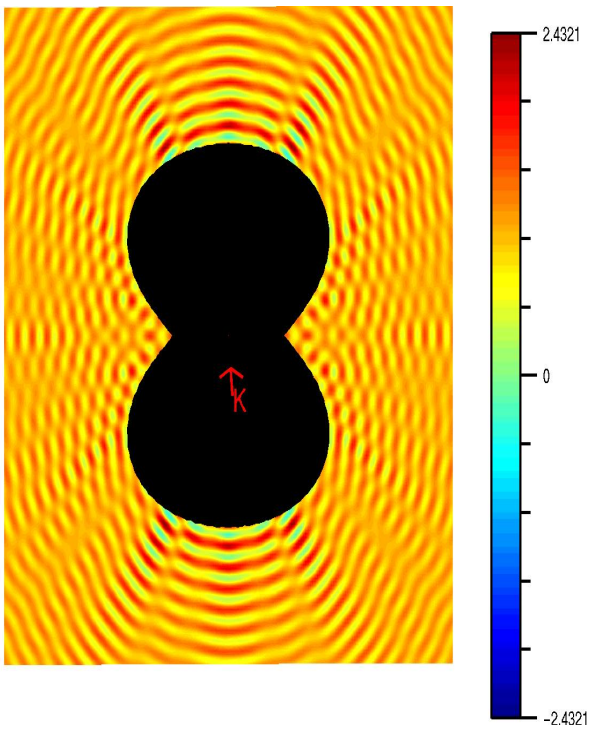

Figure 4.4: Near Field (real(u))

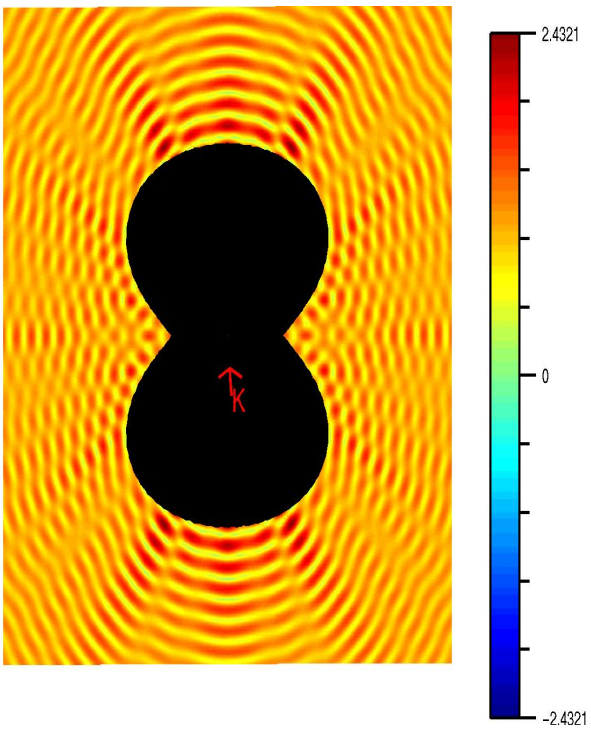

Figure 4.5:Near Field Intensity ($|u|$)